EFFECT OF N INTERSTITIALS ON THE ELECTRONIC PROPERTIES OF GaAsN ALLOY FILMS

By

Ryan M. Jock

A thesis submitted in partial fulfillment of the requirements for an
Honors Concentration in Physics
The University of Michigan
2009

*Research Advisor: Rachel S. Goldman, rsgold@umich.edu

ABSTRACT

EFFECT OF N INTERSTITIALS ON THE ELECTRONIC PROPERTIES OF GaAsN ALLOY FILMS

Ryan M. Jock

In this work, we have used rapid thermal annealing (RTA) to investigate the influence of N interstitials on the electronic properties of GaAsN alloy films. Ion beam analysis reveals an RTA-induced decrease in the concentration of N interstitials, while the total N concentration remains constant. Corresponding signatures for the reduction in interstitial N concentration are also apparent in Raman. Following RTA, both the free carrier concentration, [n], and the mobility, μ, experience a significant increase. In addition, temperature dependent transport measurements reveal a thermally activated increase in free carrier concentration at higher measurement temperatures, suggesting the presence of a carrier trapping level below the GaAsN conduction band edge. This temperature dependence is suppressed upon annealing, indicating a reduction in the concentration of the electron trapping defects after annealing. The increase in [n] following RTA suggests the association of the defects with interstitial N. Finally, annealing-dependent persistent photoconductivity (PPC) is observed in GaAsN, further suggesting a correlation between the interstitial N defect states and the electronic properties in (In)GaAsN.

To my father, for fostering my love for science,
my mother, for her constant love and support,
and my brothers Jason and Kevin

ACKNOWLEDGEMENTS

First, I would like to thank my advisor, Professor Rachel S. Goldman, and Ms. Yu Jin for their guidance and support during my research at the University of Michigan. I would also like to thank Professor Çagliyan Kurdak for valuable discussions and suggestions.

This dissertation would not have been possible without the help of my many collaborators: Mr. Hailing Cheng in the department of Physics; Mr. Tassilo Dannecker from the Tyndall Institute and University College; Cork; Dr. Yongqiang Wang from the Ion Beam Materials Laboratory (IBML) at Los Alamos Nation Laboratory, Dr. Victor Rotberg and Dr. Fabian Naab in the Michigan Ion Beam Laboratory; Dr. Alexander Mintarov, Ms. Yan He and Professor James Merz in the Department of Electrical Engineering at the University of Notre Dame.

I thank all my fellow students in the Goldman Research Group for their help. In particular, I would like to thank Jiahung and Leon for working on the MBE system with me; Rachel, Christer, Natalie and Brian, for their help with various sample characterizations.

We gratefully acknowledge the support of the National Science Foundation through a Focused Research Group (Grant No. DMR 0606406), monitored by Dr. LaVerne Hess, the Intel Foundation, and the Center for Integrated Nanotechnologies at Los Alamos National Laboratory.

Finally, I would like to thank my family and friends for their support and encouragement.

TABLE OF CONTENTS

DEDICATION……………………………………………………………………......3

ACKNOWLEDGEMENTS………………………………………………………….4

CHAPTERS

1. INTRODUCTION…………………………………………………………6
1.1 Overview……………..…………………………………….....6
1.2 Device Applications of (In)GaAsN……………………….…......7
1.3 Optical and Electronic Properties of (In)GaAsN………….......9
1.4 Persistent Photoconductivity……..……………………...….11
1.5 Nitrogen Incorporation Mechanisms……………………...…12
1.6 Thesis Objectives……….……………………………..……..13
1.7 Outline of the Dissertation…………………………….…...15
1.8 References ……………….…………………………...…...16
1.9 Figures….…………………..………………………………...19

2. EXPERIMENTAL PROCEDURES……………………………………..21
2.1 Overview…………………………………………………..21
2.2 Molecular Beam Epitaxy…………………………………….…21
2.3 Rapid Thermal Annealing………..…..………………………..…23
2.4 High-Resolution X-ray Diffraction…..……………………..…23
2.5 Ion Beam Analysis……………………………………….....24
2.6 Variable Temperature Transport Measurements..…………..…...27
2.7 Photoconductivity Measurements….….………..……….……...29
2.8 References…………………………..……………..…..…31
1.9 Figures…………………………………...……...…...32

3. RESULTS AND DISCUSSION...…………………………..……………36
3.1 Overview…………………………………….……….…….36
3.2 Background………………………………………….……..37
3.3 Nitrogen Incorporation into GaAsN…………………….……39
3.4 Transport Properties of GaAsN.............................………… 41
3.5 Persistent Photoconductivity …………………..…….….……43
3.6 Discussion..……….………………………………………..47
3.7 References………………….…………………..………...…48
3.8 Tables and Figures....……………………………………...50

4. SUMMARY AND SUGGESTIONS FOR FUTURE WORK……………60
4.1 Summary……………………...…………….…..…………60
4.2 Suggestions for Future Work…………………...………….61

1. INTRODUCTION

1.1 Overview

The dilute nitride semiconductor alloy GaAsN is promising for a wide range of device applications. The ability to substantially change the band gap energy by the addition of very small concentrations of nitrogen to (In)GaAs alloys, without significantly changing the lattice parameter, makes them useful for long-wavelength lasers[1-9] and detectors,[7] high efficiency solar cells,[1, 8, 10] and high performance heterojunction bipolar transistors.[9, 11, 12]

Figure 1.1 presents a plot of bandgap energy vs. lattice parameter for various III-V semiconductor compounds and alloys. By adding ~1% N to GaAs, the band gap energy is reduced by ~150 meV.[13-16] This significant bowing of the band gap energy enables growth of dilute nitride semiconductor alloys with a variety of band gap energies in the near-infrared range, while maintaining near-lattice-matching with common substrates such as GaAs and InP.

In this chapter, we begin with a review of the material issues arising in device applications of (In)GaAsN. This is followed by an overview of the current state of understanding of the optical and electronic properties of GaAsN. Next, the phenomenon of persistent photoconductivity is introduced. A review of the various nitrogen incorporation mechanisms in GaAsN alloys is then discussed. Finally, the chapter concludes with a presentation of the thesis objectives and outline.

1.2 Device Applications of (In)GaAsN: Material Issues

This section discusses the materials issues related to several of the device applications of (In)GaAsN. These devices include long-wavelength lasers, and detectors, high-efficiency solar cells and high performance heterojunction bipolar transistors (HBTs).

For optical data communications applications, limiting dispersion and losses is critical in the development of reliable high bit-rates and longer transmission distances. For long-wavelength vertical cavity surface-emitting lasers (VCSELs), the dilute nitride quaternary alloy $In_yGa_{1-y}As_{1-x}N_x$ (with x ~ 2%) has emerged in recent years as a very promising material for the active region. Additionally, the ability to grow InGaAsN films with a lattice parameter close to that of GaAs using methods such as molecular beam epitaxy (MBE) or metal-organic vapor phase epitaxy (MOVPE), allows for growth of quantum well laser structures on GaAs. However, the non-radiative carrier recombination centers often associated with defects in the materials characteristics strongly affect the operating characteristics of such devices.[17, 18] Therefore, understanding the nature of microstructure of the materials and the control their defects is critical to the further development of such devices.

The ability to control the band gap energy is crucial for solar cell and HBT devices. The capacity to tailor the band gap energy, E_g, of InGaAsN while leaving the lattice parameter relatively constant makes this material particularly attractive for these devices. In a solar cell, an electron-hole pair is created when photons of energy $h\nu > E_g$ are absorbed. The excess energy of each absorbed photon, $h\nu - E_g$, is dissipated as heat in

the form of phonons. Meanwhile, photons with energy, $h\nu < Eg$, are transmitted through the film. For maximum energy-conversion efficiency, a combination of materials with different band gap energies is used.[1, 8, 10] Using up to four junctions, with materials preferentially absorbing different regions of the solar spectrum, can greatly increase the device efficiency.[1, 8, 10]

In HBTs, the incorporation of dilute nitride alloys into the base layers lowers the turn on voltages and collector currents, due to the reduced band gap energy.[9, 11] An important characteristic for materials in solar cell and HBT applications is the minority diffusion length.[8, 10-12] In the case of solar cells, it limits the effective thickness of each absorbing active material layer in a multi-junction device.[10] The carrier diffusion length should be substantially longer than the optical absorption depth for photons in the window of frequencies covered by each junction in the device. This allows all incident photons to be absorbed and all optically-generated carriers to contribute to the electrical current of the device.[10] In HBTs, the carrier diffusion length should be significantly longer than the base width, in order to allow all of the carriers to contribute to the collector current.[12]

The carrier diffusion length is determined by both the carrier mobility and the recombination time.[10] Thus, for both solar cell and HBT applications, increasing the carrier mobility and recombination time is critical for the improvement of devices. For InGaAsN, electron carrier mobilities at present are typically less than 200 $cm^2/V\cdot s$, which is unacceptably low for these device applications.[19] Moreover, the defects, which contribute to scattering, also act as recombination centers, reducing the carrier diffusion length by both reducing its μ and its recombination time.[1] Therefore, if the mobility and

recombination time in this material can be increased, then substantially more efficient solar cells and higher performance HBTs could be developed.

Therefore, the electronic and optical properties of the localized structures associated with nitrogen are directly related to the effectiveness of dilute nitrides for the purposes of laser, solar cell, and transistor applications. Thus, a greater understanding of how to tailor these properties is essential to the fabrication of improved devices.

1.3 Optical and Electronic Properties of GaAsN

Shown in Fig. 1.1 is a plot of bandgap energy vs. lattice parameter for various III-V semiconductor alloys. The shaded grey region between the two data points for InN indicates the uncertainty in the bandgap energy for InN. The red line between GaAs and InAs shows the InGaAs bandgap energy, which decreases with increasing indium composition. As shown in Fig. 1.1, GaN has a much larger bandgap energy than GaAs and a linear interpolation of the bandgap energy would predict that the bandgap energy $GaAs_{1-x}N_x$ would increase with increasing nitrogen composition. However, as predicted theoretically and seen experimentally, this is not the case.[14, 15 19-21] The GaAsN alloy bandgap energy is given by

$$E_g(GaAs_{1-x}N_x) = x \cdot E_g(GaN) + (1-x) \cdot E_g(GaAs) + b \cdot x \cdot (1-x)$$

where b is a widely debated bowing parameter.[14, 22-26] The green line in Fig. 1.1 between GaAs and GaN shows the resulting GaAsN bandgap energy, assuming a composition dependent bowing parameter. In addition, in Fig. 1.1, the red line between GaAs and InAs shows the InGaAs bandgap energy, which decreases with increasing indium

composition. Finally, the blue line in Fig. 1.1 shows the potential bandgap energies for $In_yGa_{1-y}As_{1-x}N_x$ lattice-matched to GaAs, where the alloy is grown with a 3 to 1 N to In concentration ratio.

Recently, there have been considerable theoretical and experimental studies to understand the origins of band gap bowing in GaAsN alloys. Several models have been proposed, including the two-band crossing (BAC),[27] the multiband hybridization,[28, 29] and the N-impurity band formation models. [30, 31] In the BAC model, anti-crossing between the localized N impurity level and the extended states of the GaAs matrix splits the conduction band into two sub-bands, referred to as E_+ and E_-,[27] where the lower Energy band, E_-, is the alloy conduction band edge.[27] In the multiband hybridization model N disorder leads to both perturbed host states as well as cluster states resulting.[28, 29] Lastly, in the N-impurity band model, overlapping states result from heavy N doping, which creates an impurity band within the band gap, thus decreasing the conduction band with increasing N doping concentration.[30,31] Additionally, various N-related transitions observed at different N concentrations are typically associated with different N-pair and -cluster states, although these conclusions are unclear or controversial.[23, 32-36]

The N-related shallow donor defect level discussed above may correspond to shallow electron traps in GaAsN reported in literature using various experimental methods. With capacitance spectroscopy, Krispin et al found a composition independent electron trap about 1.1eV above the valence band edge.[37] Kurtz el al found a trap 0.18 to 0.25eV below the conduction-band edge by DLTS.[8] Kaplar et al reported shallow electron traps with an activation energy of 0.14eV in Sn-doped n-type GaInNAs using DLTS. In addition, first principle calculations suggest the existence of N-related defect

states below GaAsN conduction band, the positions of which do not change with N composition.[38-40]

To date, literature reports as-grown (In)GaAsN films exhibiting optical emission efficiency and electron mobilities that are significantly lower than those of (In)GaAs. In addition, the electron mobility and optical emission efficiency have been reported to decrease as the N incorporation in (In)GaAsN increases.[7, 41, 42] Post-growth rapid thermal annealing (RTA) has been extensively used to improve the photoluminescence (PL) efficiency of (In)GaAsN.[43-45] This improvement has commonly been attributed to the elimination of some grown-in competing non-radiative channels. The exact mechanism, however, is not fully understood [43, 46] and reports on the effect of annealing on transport property of (In)GaAsN are very limited.[19, 47]

1.4 Persistent Photoconductivity

Persistent photoconductivity (PPC) refers to a phenomenon in which an illumination induced increase in conductivity persists for a significant time, usually on the order of hours or even days, following the cessation of illumination. PPC has been observed in various compound semiconductors systems, such as AlGaAs, InP, GaAsP, GaAsSb, AlGaN, and more recently, in materials other than semiconductors, such as polycrystalline Si, Ge, and Carbon nanotubes.

The PPC effect has been attributed to a potential barrier, which prevents the recombination of photo-generated non-equilibrium electrons and holes. The behavior of the recombination potential barrier, until now, has not been fully understood. Various

theories have been proposed, including large lattice relaxation, a microscopic random-potential induced by defect clusters, donor clusters, or intentionally designed structures, such as modulation doped heterostructures.[48-51] In this model, the recapture of electrons by the deep levels is hindered by a thermal barrier at low temperatures, thus resulting in an prolonged increase in carrier concentration in the material and PPC.[48, 49]

PPC has been observed by several groups and has been ascribed to deep centers.[52, 53] Hsu et al. and Li et al. attribute this phenomenon to N-induced defects undergoing large lattice relatxation upon photoexcitation.[52, 53] However, an explanation for the origin of the PPC effect, has not yet been proposed.

1.5 Nitrogen Incorporation Mechanisms

As discussed in Section 1.2, the incorporation of N into (In)GaAs introduces a significant decrease in the band gap,[13-16], making (In)GaAsN, a promising material for a wide range of applications.[1-8, 10] However, one of the main limitations of (In)GaAsN in devices is that the incorporation of nitrogen degrades the electronic and optical properties.[1, 4, 8, 10, 37, 54, 55] This degradation has been attributed to N-related point defects which act as non-radiative, lifetime-killing centers.[37, 54, 55] In the case of GaAsN, N-induced recombination and/or trapping centers are likely responsible for drastically reducing the electron and hole mobilities[56] and minority carrier lifetime,[54, 55] leading to poor device performance. However, the types and relative concentrations of point defects in GaAsN are widely debated.[17, 37, 57-61] Thus, further studies of the mechanisms of N

incorporation in GaAsN can lead to a greater understanding of the degradation of the optical and electronic properties with increasing N incorporation.

Several possible nitrogen induced defects are shown in Fig. 1.2.[56] For substitutional nitrogen, N_{As} , a nitrogen atom takes the place of an arsenic atom, as shown in Fig. 1.2 (a). The N-N split interstitial complex, NN_{split} , for which an N_2 molecule takes the place of an As atom, is shown in Fig. 1.2 (b). [57, 58] For the N-As split interstitial complex, NAs_{split}, a nitrogen and arsenic atom are both located on the As lattice site, as shown in Fig. 1.2 (c).[57, 58] For NAs_{split}, the calculated minimum energy configuration involves the As atom located in the center of the group V site, with the N atom offset by 0.6 Å.25 Fig. 1.2 (d) and (e) show the $(As_{Ga}\text{-}N_{As})_{nn}$ and $(V_{Ga}\text{-}N_{As})_{nn}$ complexes, respectively, where *nn* stands for nearest neighbor.[57] For these complexes, a nitrogen atom substitutes for an arsenic atom similar to N_{As}, but the nearest neighbor Ga lattice site is either an arsenic anti-site, As_{Ga} , or vacancy, V_{Ga} .[57]

1.6 Thesis Objectives

As discussed in Section 1.2, Group III-V-N alloys such as GaAsN and (In)GaAsN with a few percent nitrogen have shown significant promise for a wide range of applications. However, in as-grown (In)GaAsN films, the electron mobility and optical emission efficiency are observed to decrease as the nitrogen incorporation increases.[7, 41, 42] As suggested by the calculations of Zhang et al,[37, 39] a significant fraction of N atoms are expected to be incorporated non-substitutionally, such as NN split interstitials, $(NN)_{As}$, or NAs split interstitials, $(NAs)_{As}$. Direct measurements of the fraction of N

incorporated interstitially, f_{int}, via nuclear reaction analysis (NRA) have been reported by several groups[17, 59, 62, 63] It has been suggested that post-growth rapid thermal annealing (RTA) reduces f_{int}.[17, 37, 59, 64] However direct evidence for the RTA effect on f_{int} in GaAsN is limited to single data points in two literature reports.[17, 59] Furthermore, despite the extensive number of studies on the effect of RTA on the optical properties of (In)GaAsN, studies of the effect of RTA on the electronic properties of (In)GaAsN are limited.

Corresponding signatures for the reduction in interstitial N concentration are seen in Raman spectra. In this work, we provide direct evidence of the reduction in f_{int} by the NRA, thus proving that these Raman signatures are due to N interstitials. Transport measurements reveal a remarkable improvement in electronic properties after annealing. Furthermore, variable temperature magnetoresistance measurement reveal a thermally activated increase in free carrier concentration up to room temperature, suggesting the existence of an electron trap level below the conduction band edge, the concentration of which is reduced by annealing. The correlation between the reduction in f_{int} and the improvement in transport properties of GaAsN suggests that interstitial N-related defects act as electron trapping/scattering centers, which can be substantially suppressed by RTA. Additionally, we have observed the persistent photoconductivity (PPC) effect in GaAsN, which is suppressed by rapid thermal annealing (RTA). Similarities in the behavior of N-related defects in GaAsN and DX-centers in AlGaAs can be used to interpret the nature of their microstructure. In this work it is shown that post-growth rapid thermal annealing (RTA) can be used to control the interstitial nitrogen fraction. Therefore, we have utilized RTA to probe the influence of interstitial N on the electronic properties of GaAsN alloy films.

1.7 Outline of Thesis

The thesis is organized as follows. Chapter 2 describes the experimental procedures used for this work, including molecular beam epitaxy (MBE) growth, Rutherford backscattering (RBS), nuclear reaction analysis (NRA), x-ray rocking curves (XRC), variable temperature Hall transport measurements, and persistent photoconductivity (PPC) measurements.

Chapter 3 discusses the study of the effect of N interstitials on the electronic properties of GaAsN. The correlation between annealing temperature, interstitial N faction and the transport properties is discussed. Mobility and free carrier concentrations are examined using variable temperature Hall and magnetoresistance measurements for GaAsN alloys both as-grown and after annealing. Furthermore, the persistent photoconductivity effect in GaAsN films is also discussed.

In chapter 4, a summary and suggestions for future work are presented.

1.8 References and Figures

[1]I. A. Buyanova, W. M. Chen, and B. Monemar, Mrs Internet Journal of Nitride Semiconductor Research **6,** (2001).
[2]M. Fischer, D. Gollub, and A. Forchel, Japanese Journal of Applied Physics Part 1-Regular Papers Short Notes & Review Papers **41,** 1162 (2002).
[3]D. Gollub, S. Moses, and A. Forchel, Electronics Letters **40,** 1181 (2004).
[4]J. S. Harris, Semiconductor Science and Technology **17,** 880 (2002).
[5]L. H. Li, V. Sallet, G. Patriarche, L. Largeau, S. Bouchoule, K. Merghem, L. Travers, and J. C. Harmand, Electronics Letters **39,** 519 (2003).
[6]G. Steinle, F. Mederer, M. Kicherer, R. Michalzik, G. Kristen, A. Y. Egorov, H. Riechert, H. D. Wolf, and K. J. Ebeling, Electronics Letters **37,** 803 (2001).
[7]M. R. Gokhale, J. Wei, H. S. Wang, and S. R. Forrest, Applied Physics Letters **74,** 1287 (1999).
[8]S. R. Kurtz, A. A. Allerman, E. D. Jones, J. M. Gee, J. J. Banas, and B. E. Hammons, Applied Physics Letters **74,** 729 (1999).
[9]P. C. Chang, N. Y. Li, A. G. Baca, H. Q. Hou, C. Monier, J. R. Laroche, F. Ren, and S. J. Pearton, Ieee Electron Device Letters **22,** 113 (2001).
[10]J. F. Geisz, and D. J. Friedman, Semiconductor Science and Technology **17,** 769 (2002).
[11]C. Monier, A. G. Baca, P. C. Chang, N. Y. Li, H. Q. Hou, F. Ren, and S. J. Pearton, Electronics Letters **37,** 198 (2001).
[12]P. M. Asbeck, R. J. Welty, C. W. Tu, H. P. Xin, and R. E. Welser, Semiconductor Science and Technology **17,** 898 (2002).
[13]S. G. Spruytte, M. C. Larson, W. Wampler, C. W. Coldren, H. E. Petersen, and J. S. Harris, Journal of Crystal Growth **227,** 506 (2001).
[14]W. G. Bi, and C. W. Tu, Applied Physics Letters **70,** 1608 (1997).
[15]K. Uesugi, N. Morooka, and I. Suemune, Applied Physics Letters **74,** 1254 (1999).
[16]U. Tisch, E. Finkman, and J. Salzman, Applied Physics Letters **81,** 463 (2002).
[17]S. G. Spruytte, C. W. Coldren, J. S. Harris, W. Wampler, P. Krispin, K. Ploog, and M. C. Larson, Journal of Applied Physics **89,** 4401 (2001).
[18]W. Li, M. Pessa, and J. Likonen, Applied Physics Letters **78,** 2864 (2001).
[19]K. Volz, J. Koch, B. Kunert, and W. Stolz, Journal of Crystal Growth **248,** 451 (2003).
[20]L. Bellaiche, S. H. Wei, and A. Zunger, Physical Review B **54,** 17568 (1996).
[21]Y. Zhao, F. Deng, S. S. Lau, and C. W. Tu, Journal of Vacuum Science & Technology B **16,** 1297 (1998).
[22]L. Bellaiche, S. H. Wei, and A. Zunger, Applied Physics Letters **70,** 3558 (1997).
[23]T. Makimoto, H. Saito, T. Nishida, and N. Kobayashi, Applied Physics Letters **70,** 2984 (1997).
[24]G. Pozina, I. Ivanov, B. Monemar, J. V. Thordson, and T. G. Andersson, Journal of Applied Physics **84,** 3830 (1998).
[25]J. Salzman, and H. Temkin, Materials Science and Engineering B-Solid State Materials for Advanced Technology **50,** 148 (1997).
[26]S. Francoeur, G. Sivaraman, Y. Qiu, S. Nikishin, and H. Temkin, Applied Physics Letters **72,** 1857 (1998).

[27]W. Shan, W. Walukiewicz, J. W. Ager, E. E. Haller, J. F. Geisz, D. J. Friedman, J. M. Olson, and S. R. Kurtz, Physical Review Letters **82,** 1221 (1999).
[28]P. R. C. Kent, and A. Zunger, Physical Review B **64,** (2001).
[29]P. R. C. Kent, and A. Zunger, Physical Review Letters **86,** 2613 (2001).
[30]Y. Zhang, A. Mascarenhas, J. F. Geisz, H. P. Xin, and C. W. Tu, Physical Review B **63,** (2001).
[31]Y. Zhang, A. Mascarenhas, H. P. Xin, and C. W. Tu, Physical Review B **61,** 7479 (2000).
[32]Y. Zhang, A. Mascarenhas, H. P. Xin, and C. W. Tu, Physical Review B **61,** 4433 (2000).
[33]P. J. Klar, H. Gruning, W. Heimbrodt, J. Koch, F. Hohnsdorf, W. Stolz, P. M. A. Vicente, and J. Camassel, Applied Physics Letters **76,** 3439 (2000).
[34]B. A. Weinstein, S. R. Stambach, T. M. Ritter, J. O. Maclean, and D. J. Wallis, Physical Review B **68,** (2003).
[35]X. D. Luo, J. S. Huang, Z. Y. Xu, C. L. Yang, J. Liu, W. K. Ge, Y. Zhang, A. Mascarenhas, H. P. Xin, and C. W. Tu, Applied Physics Letters **82,** 1697 (2003).
[36]S. Francoeur, S. A. Nikishin, C. Jin, Y. Qiu, and H. Temkin, Applied Physics Letters **75,** 1538 (1999).
[37]P. Krispin, V. Gambin, J. S. Harris, and K. H. Ploog, Journal of Applied Physics **93,** 6095 (2003).
[38]A. Lindsay, and E. P. O'Reilly, Phys. Rev. Lett. **93,** (2004).
[39]S. B. Zhang, and S.-H. Wei, Phys. Rev. Lett. **86,** 1789 (2001).
[40]P. R. C. Kent, and A. Zunger, Physica Status Solidi B-Basic Research **228,** 253 (2001).
[41]I. A. Buyanova, W. M. Chen, and C. W. Tu, Semiconductor Science and Technology **17,** 815 (2002).
[42]J. S. Wang, A. R. Kovsh, L. Wei, J. Y. Chi, Y. T. Wu, P. Y. Wang, and V. M. Ustinov, Nanotechnology **12,** 430 (2001).
[43]I. A. Buyanova, G. Pozina, P. N. Hai, N. Q. Thinh, J. P. Bergman, W. M. Chen, H. P. Xin, and C. W. Tu, Applied Physics Letters **77,** 2325 (2000).
[44]L. H. Li, Z. Pan, W. Zhang, Y. W. Lin, Z. Q. Zhou, and R. H. Wu, Journal of Applied Physics **87,** 245 (2000).
[45]W. K. Loke, S. F. Yoon, S. Z. Wang, T. K. Ng, and W. J. Fan, Journal of Applied Physics **91,** 4900 (2002).
[46]Q. D. Zhuang, A. Krier, and C. R. Stanley, Journal of Applied Physics **101,** (2007).
[47]F. Ishikawa, G. Mussler, K. J. Friedland, H. Kostial, K. Hagenstein, L. Daweritz, and K. H. Ploog, Applied Physics Letters **87,** (2005).
[48]H. X. Jiang, and J. Y. Lin, Physical Review B **40,** 10025 (1989).
[49]D. E. Theodorou, and C. I. Symeonidis, Physical Review B **37,** 10854 (1988).
[50]D. V. Lang, and R. A. Logan, Physical Review Letters **39,** 635 (1977).
[51]H. J. Queisser, and D. E. Theodorou, Physical Review B **33,** 4027 (1986).
[52]S. H. Hsu, W. R. Chen, Y. K. Su, R. W. Chuang, S. J. Chang, and W. C. Chen, Journal of Crystal Growth **290,** 87 (2006).
[53]J. Z. Li, J. Y. Lin, H. X. Jiang, J. F. Geisz, and S. R. Kurtz, Applied Physics Letters **75,** 1899 (1999).
[54]J. F. Geisz, D. J. Friedman, J. M. Olson, S. R. Kurtz, and B. M. Keyes, Journal of Crystal Growth **195,** 401 (1998).

[55]D. Kwon, R. J. Kaplar, S. A. Ringel, A. A. Allerman, S. R. Kurtz, and E. D. Jones, Applied Physics Letters **74,** 2830 (1999).
[56]
[57]S. B. Zhang, and S. H. Wei, Physical Review Letters **86,** 1789 (2001).
[58]E. Arola, J. Ojanen, H. P. Komsa, and T. T. Rantala, Physical Review B **72,** (2005).
[59]T. Ahlgren, E. Vainonen-Ahlgren, J. Likonen, W. Li, and M. Pessa, Applied Physics Letters **80,** 2314 (2002).
[60]P. Wei, M. Chicoine, S. Gujrathi, F. Schiettekatte, J. N. Beaudry, R. A. Masut, and P. Desjardins, Journal of Vacuum Science & Technology A **22,** 908 (2004).
[61]H. C. Alt, A. Y. Egorov, H. Riechert, J. D. Meyer, and B. Wiedemann, Physica B-Condensed Matter **308,** 877 (2001).
[62]M. Reason, H. A. McKay, W. Ye, S. Hanson, R. S. Goldman, and V. Rotberg, Appl. Phys. Lett. **85,** 1692 (2004).
[63]H. C. Alt, A. Y. Egorov, H. Riechert, B. Wiedemann, J. D. Meyer, R. W. Michelmann, and K. Bethge, Physica B **302,** 282 (2001).
[64]H. F. Liu, N. Xiang, and S. J. Chua, Journal of Crystal Growth **290,** 24 (2006).

1.9 Figures

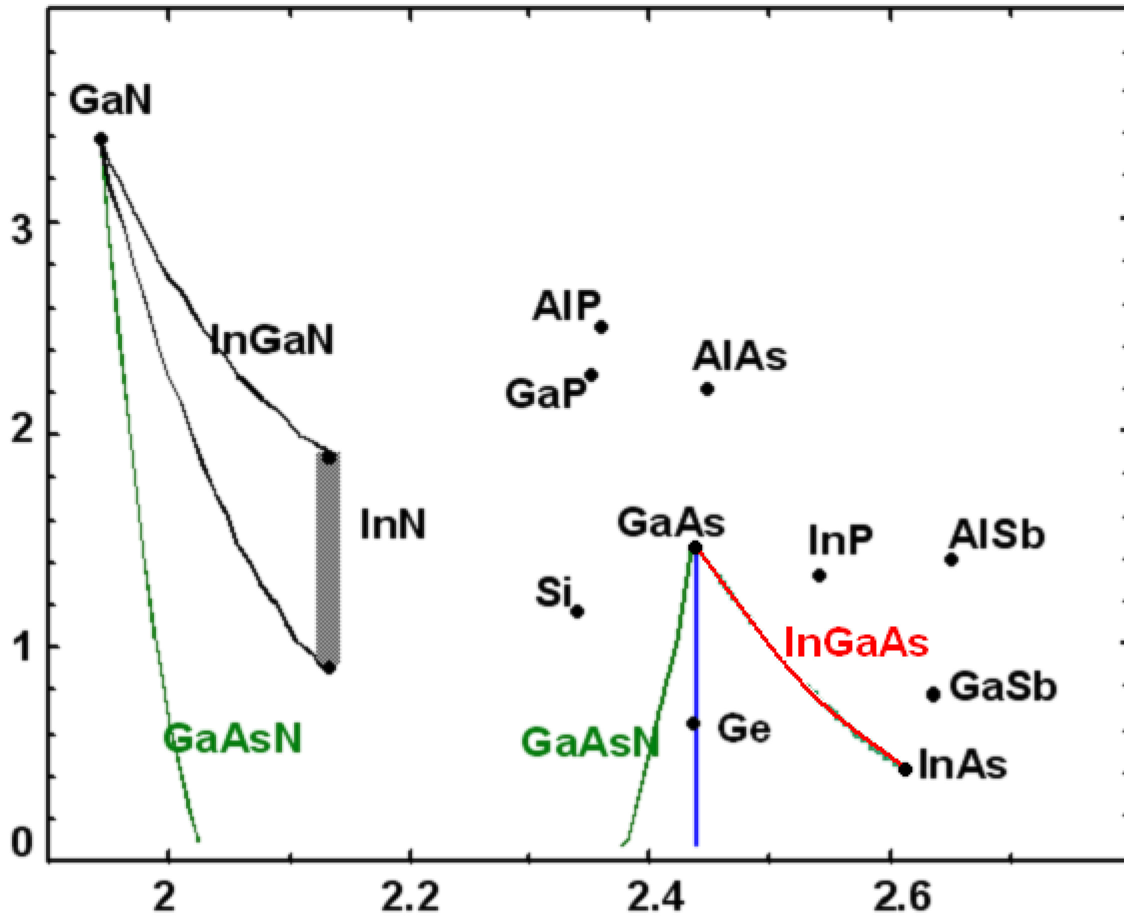

Figure 1.1: A plot of bandgap energy vs. lattice parameter for various III-V semiconductor compounds and alloys represented by the black dots. The green line between GaAs and GaN shows the resulting GaAsN bandgap energy. The red line between GaAs and InAs shows the InGaAs bandgap energy, which decreases with increasing indium composition. The shaded grey region between the two data points for InN indicates the uncertainty in the bandgap energy for InN. Finally, the blue line shows the potential bandgap energies for $In_yGa_{1-y}As_{1-x}N_x$ lattice-matched to GaAs, where the alloy is grown with a 3 to 1 N to In concentration ratio.

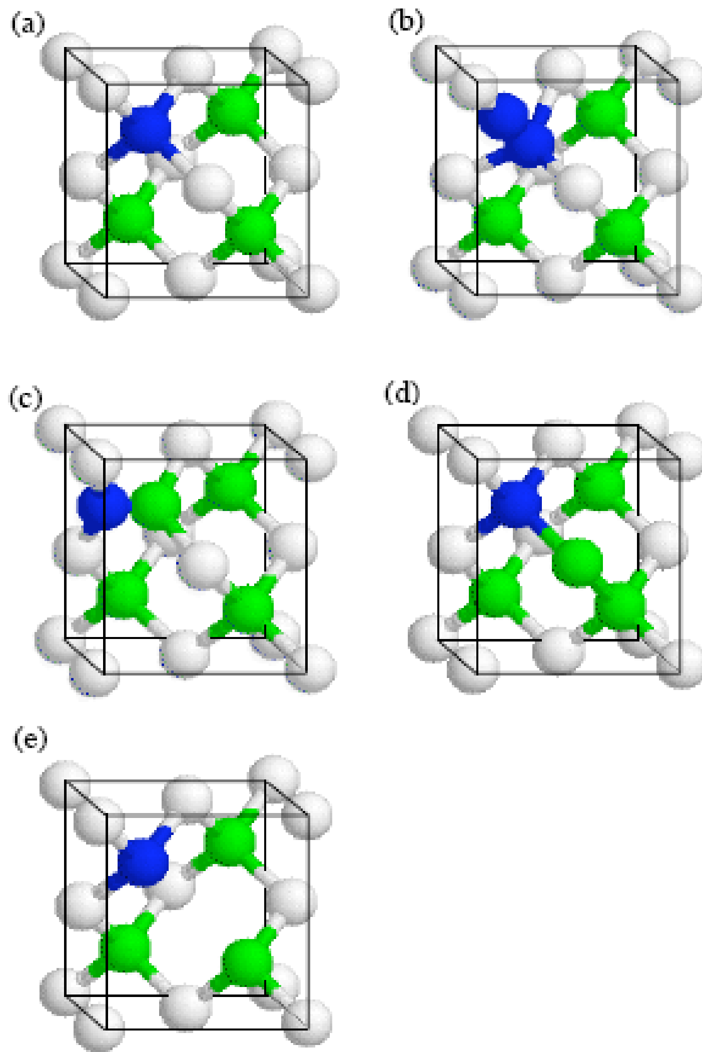

Fig. 1.2: Schematics for the GaAs unit cell containing several N induced defects, The white, green (grey), and blue (black) spheres represent Ga, As, and N, respectively.

(a) substitutional N, N_{As} ,
(b) N-N split interstitial, NN_{split} ,
(c) N-As split interstitial, NAs_{split} ,
(d) $(As_{Ga}\text{-}N_{As})_{nn}$ complex
(e) $(V_{Ga}\text{-}N_{As})_{nn}$ complex.

2. EXPERIMENTAL PROCEDURES

2.1 Overview

This chapter describes the procedures used for the synthesis and characterization of GaAsN alloy films. Films were grown on semi-insulating GaAs (001) substrates by molecular-beam epitaxy (MBE). Following the growth, x-ray rocking curve (XRC) measurements were performed to determine nitrogen composition. Ion beam analysis was performed in order to study nitrogen incorporation mechanisms. Lastly, variable temperature transport and persistent photoconductivity (PPC) measurements were performed in order to investigate optical and electronic properties of the films.

2.2 Molecular-Beam Epitaxy

Molecular-beam epitaxy is a vacuum evaporation process, performed at ultra-high vacuum, and is used to prepare high quality epitaxial films one atomic layer at a time.[1] Molecular beams are produced by evaporation or sublimation from heated liquids or solids. These beams interact chemically on the substrate by condensation of the elemental components and form an epitaxial film.[2] Samples for this research were grown by Ms. Yu Jin and other members of the Goldman Research Group.

Films were grown in a modified Varian Gen II chamber, shown schematically in Fig. 2.1. This system consists of a separately pumped growth chamber, buffer chamber, and load-lock and samples are moved between sections using magnetic transfer rods and

trolleys. The growth chamber source flange contains several sources (In, Ga, Al, Si, Te, and As), as well as an RF plasma source for the creation of active N from an ultrahigh purity mixture of 10% N_2/Ar gas. Another source flange contains a residual gas analyzer (RGA) for *in-situ* mass spectroscopy. The sources are held in pyrolytic boron nitride (PBN) crucibles encased in Knudsen cells. A purity of 99.99999% (7N) for In, Ga, and As material and 99.99995% for Al is used. Computer controlled pneumatic shutters regulate the exposure of the samples to each molecular beam. During growth, samples are held in place by the manipulator reffered to as the CAR (for Continuous Azimuthal Rotation). The CAR may be rotated during growth to improve uniformity. This growth chamber contains facilities for *in-situ* reflection high-energy electron diffraction (RHEED) and a multi-beam optical stress sensor (MOSS). RHEED and MOSS are used to study the surface morphology and stress evolution, respectively, of GaAsN films before, during and after growth.

The GaAsN alloy films were grown on semi-insulating (001) GaAs substrates, using Ga, As_2 or As_4, Si or GaTe (for n-type doping) and the N_2 RF plasma source discussed above. Due to their high vapor pressure, group VI elemental sources are generally not suitable for MBE.[3] However, chalcogenides such as GaTe has been shown to be a well-behaved dopant for GaAs, with minimal cross-talk or memory effects.[3, 4] The Si and GaTe cell temperatures were chosen to target free carrier concentrations of $1x10^{18}cm^{-3}$ in GaAs:Te and GaAs:Si control samples. Most GaAsN samples were grown at relatively low temperature (400-425°C), to avoid growth in the so called Forbidden Window, which is a specific temperature range where multilayer growth occurs, surrounded by layer-by-layer growth region.[5] Several GaAsN samples were also grown

at, 550-580°C, which will be referred to as high T grown samples. Substrates were mounted on heated molybdenum blocks with indium. Samples were pre-baked in the load-lock at 150°C for 8 hours. The samples were then outgassed at 180°C in the buffer chamber for 30 minutes. In the growth chamber, the substrate temperature was raised until a transition from diffuse rings to a streaky (2x4) pattern was observed in the RHEED, indicating the surface oxide had desorbed. After desorption of the oxide, the samples were outgassed under As_2 at 610°C for 10 minutes.

2.3 Rapid Thermal Annealing

For selected samples, post-growth rapid thermal annealing was performed in a RTP150 with a quartz lamp as the heat source at Michigan Solid State Electronic Labotary (SSEL). Samples were annealed at 700-800˚C for 60s in N_2 ambient, with a GaAs proximity cap to prevent As out-diffusion.

2.4 High-Resolution X-Ray Diffraction

Double-axis x-ray curves (XRC) were performed on bulk GaAsN films before and after annealing to determine the nitrogen composition in these films. All XRC measurements were carried out using a BEDE D[1] System, shown schematically in Fig. 2.2.[2] This system used a 2.2 kW filament tube with a copper target. X-rays were monochromated by two Si channel cut crystals. These crystals were oriented to select the CuKα line with a beam divergence of 12 arcseconds.[2, 6] A vertical slit of width 5 mm and

a circular slit of radius 5 mm were inserted in the path of the beam in order to center the beam and reduce background scattering, as shown schematically in Fig. 2.2. At the sample position, the resulting x-ray spot size was typically 0.5 x 20 mm. Generator settings of 40 mA and 40 kV were used, resulting in a typical direct beam intensity of ~200,000 counts per second. Samples were mounted on the sample stage using vacuum grease, which is easily removed using successive rinses of acetone and isopropanol. The sample stage was mounted on a goniometer, which allows movement about three axes, rocking (ω), tilting (χ), and azimuthal rotation (φ), as shown in Fig. 2.2. A wide-angle detector was used to collect the signal.

For the XRC measurements, two sets of reflections were measured; the symmetric (004) and the asymmetric and the glancing-incidence (224). Each set of measurements was performed at azimuthal angles of 0° and 180° as a means to average out the measurement. In order to determine the epilayer-substrate peak separation, the peak positions were determined using curve fitting with Kaleidagraph. Gaussian and Lorentzian curves were fitted to each peak, and the method with the R-value (multiple-correlation coefficient) closest to unity was chosen, as described in Matt Reason's 2006 dissertation, Structure and Properties of Dilute Nitride GaAsN alloy Films.[2]

2.5 Ion Beam Analysis

The total N concentration and the fraction of substitutional N incorporation, *f*, in GaAsN films were determined using ion beam analysis techniques. The total N concentration was determined from nuclear reaction analysis (NRA) measurements in

non-channeling conditions. A combination of Rutherford backscattering (RBS) and NRA were used, in both channeling and non-channeling conditions, to determine *f*.[7] Dr. Wang at LANL performed some of the measurements using a 3.2 MV tandem ion accelerator and a beam line analysis chamber, which is equipped with a five-axis, computer-controlled goniometer for sample changing and channeling measurements.. The rest of the measurements were performed the Michigan Ion Beam Laboratory (MIBL), using a general Ionex 1.7 MV Tendetron accelarator[8].

Figure 2.3 shows a schematic of the RBS experiment.[2] In this set up, negatively charged ${}_2^4He$ were produced by a duoplasmatron and were then converted into α-particles as they passed through a charge exchange canal.[2] The α-particles were then accelerated to an energy of 2 MeV. A collimated beam of these particles was directed at the surface of a GaAs reference sample. Elastically scattered ions were collected by a charged-particle radiation detector of solid angle Ω=5 milli-steradians (msr), as shown by the dashed lines in Fig. 2.3 The detector was mounted at a scattering angle of θ=170° in order to maximize the number of ions detected, without blocking the incoming ion beam[2]. By collecting the charge pulse created by the conversion of energy from the detected α-particle to electron-ion pairs, and multiplying by the effective ionization potential required to produce each pair, the detector determined the energy of each scattered α-particle, with a resolution of ~2 keV.[2]

The total number of incident ions, Q, was measured by a charge integrator (a capacitor, transistor, and pulse counter connected in parallel), which was electrically connected to the sample. As the incoming particles reached the sample, their charge was transferred to the sample, and then collected by the capacitor. Once the voltage across the

capacitor reached a set value, the transistor allowed the capacitor to discharge completely. The pulse counter then counted each pulse of current from the capacitor and the total incoming charge was determined by multiplying the number of pulses by the charge per pulse. A Faraday cup was used to produce an electric field around the sample.[2] This forced sputtered electrons back to the sample, and prevent them from being measured as incident positive charge.

In the NRA experiment, shown schematically in Fig. 2.3, positively charged Deuterons, *d*, were created by a TORVIS ion source.[2] The deuterons were then accelerated to an energy of 1.4 MeV and collimated into a beam which was directed at the GaAsN sample surface. The incident deuterons have a penetration depth of ~15 μm, which is much greater than the thickness of our GaAsN films.[2] The energies and total numbers of the emitted particles for each reaction were measured using a 5 msr detector, mounted at a scattering angle θ=150°. At this angle the scattering cross-section for the $^{14}N(d,\alpha)^{12}C$ reaction is known24. A 24 μm mylar film was placed in front of the detector to filter out backscattered deuterons and prevent saturation of the detector.[2] The charge integrator was used to measure the incoming charge, Q.

RBS was performed in channeling and non-channeling conditions on MBE-grown GaAs reference samples. NRA measurements were performed in both channeling and non-channeling conditions on MBE-grown GaAsN samples. All sets of channeling and non-channeling measurements were performed multiple times for improved accuracy. These measurements were performed on the same sample location and revealed negligible lattice damage induced by the deuteron beam. The GaAs RBS reference measurements were then used in conjunction with NRA measurements on GaAsN films

to calculate the fraction of substitutional N. In addition, the total N concentration for each sample is determined from the NRA yield in the non-channeling condition.

2.6 Variable Temperature Transport Measurements

Electron transport measurements were implemented in both the Van der Pauw and Hall bar geometries in a variable temperature cryostat. The electron mobilities and free carrier concentrations of GaAsN films were investigated using variable temperature Hall and magnetoresistance measurements at temperatures ranging from 1.6 to 300 K. These measurements were performed by Ryan Jock and/or Yu Jin in Professor Kurdak's Lab at the University of Michigan.

Figure 2.4 shows a schematic of the symmetric van der Pauw geometry, which was used for a majority of the measurements in this work.[2] Indium contacts, ~0.5 mm diameter, were deposited on the corners of a ~5 mm x ~5 mm square sample. The samples were then annealed at 410°C for 2 min to allow the indium to diffuse into the layers to form Ohmic contacts. Gold wires of 25 μm diameter were then bonded to each contact, and soldered to the sample mount. The Ohmic nature of all contacts was verified using a Hewlett Packard 4156B precision semiconductor parameter analyzer, with the contact resistance in the range of 1-10 kΩ.

The samples were loaded into the sample camber of the variable temperature cryostat depicted in Fig. 2.5. The sample chamber of the cryostat was kept near vacuum by an Edwards mechanical vacuum pump. The next chamber of the cryostat was filled with liquid helium. The temperature was controlled by allowing small amounts of He gas,

near liquid He temperatures, to flow through a valve into the sample chamber, pumping on the sample chamber with the vacuum pump, and using a heating coil, which was controlled by a LakeShore 340 Temperature Controller. The temperature controller also monitored the temperature near the sample within the chamber. Inside the cryostat is a superconducting magnet, whose field was controlled by either a LakeShore Magnet Power Supply or a AMI Model 420 Power Supply along with a AMI Model 601 Energy Absorber.

For the resistivity measurements, the voltage drop parallel to the current was measured in the absence of a magnetic field. For the Hall measurements, the voltage drop perpendicular to the current was measured in the presence of a magnetic field. From these measurements, the electron mobility, μ, and free carrier concentration, [n], were determined using standard Hall measurement procedures.[2, 8] For these measurements, low noise lock-in amplifiers were used in order to monitor both the in-phase and out-of-phase components of the resistivity. When the out-of-phase component is comparable to the in-phase component, we knew that the measurements were no longer meaningful. A voltage of 5 V was sent though a 10-100 MΩ resister, at a random, non-integer frequency in the range of 10 to 50 Hz, though the sample, then was connected to ground. The difference in voltage across the sample was measured by the same lock-in amplifier, whose signal was then monitored by an Agilent 34401A Digital Multimeter. The voltage across the superconducting magnet was also monitored by an Agilent 34401A Digital Multimeter. Using LabView, we monitored these multimeters and by sweeping the magnetic field forward and backward between 0 and ~7 T, we obtained a plot of voltage across the

sample vs. current through the magnet. This we could calibrate to obtain a graph of resistance vs. magnetic field, at various temperatures.

2.7 Persistent Photoconductivity Measurements

To study the persistent photoconductivity in GaAsN, we performed three experiments. These measurements were performed in the same cryostat and with the same lock-in amplifiers as described in the previous section. Samples were loaded with a near-infrared light emitting diode (LED) with emitting wavelength 940~950 nm, the current through which was controlled by a power supply.

In the first experiment, the temperature was ramped down to between 5 and 1 K. The LED was then turned on until the resistivity remained constant with further illumination, or saturated, then was turned off. Transport measurements were then performed in the same manner as described in the previous section. For consistency, [n] and μ after illumination are all measured after LED had been turned off for 3 minutes. This was then repeated at higher temperatures by ramping up the temperature and turning on the LED until the resistivity was again saturated.

To study the mechanism of relaxation of the PPC, the resistivities of GaAsN samples were measured at different temperatures as a function of time before, during and after illumination with the LED, . The sample chamber was ramped down to predetermined temperature in dark, the LED was turned on until the resistivity saturated, then turned off. Following the termination of illumination, the time-dependence of the resistivities of GaAsN samples were monitored. The temperature was then ramped up to

230 K and annealed for 10 minutes to ensure that the sample recover to the equilibrium dark state. The temperature was then ramped down to the next prescribed temperature and this illumination and measurements were repeated.

Lastly, we measured the mobility as a function of free carrier concentration at 40 and 80 K. This was done by first measuring the mobility and free carrier concentration on the samples in dark. To increase the bumber of photoexcited carriers the samples were then briefly illuminated with the LED, followed by transport measurements in the dark. This was repeated until the free carrier concentration of the sample remained constant with further illumination.

2.8 References

[1]A. Y. Cho, Journal of Crystal Growth **201,** 1 (1999).
[2]M. Reason, thesis, University of Michigan, 2006
[3]A. Furukawa, and M. Mizuta, Electronics Letters **24,** 1378 (1988).
[4]B. R. Bennett, R. Magno, and N. Papanicolaou, Journal of Crystal Growth **251,** 532 (2003).
[5]M. Reason, N. G. Rudawski, H. A. McKay, X. Weng, W. Ye, and R. S. Goldman, Journal of Applied Physics **101,** 083520 (2007).
[6]Z. Pan, Y. T. Wang, L. H. Li, W. Zhang, Y. W. Lin, Z. Q. Zhou, and R. H. Wu, Journal of Crystal Growth **217,** 26 (2000).
[7]M. Reason, H. A. McKay, W. Ye, S. Hanson, R. S. Goldman, and V. Rotberg, Applied Physics Letters **85,** 1692 (2004).
[8]Y. Jin, thesis, University of Michigan, In Preparation

2.9 Figures

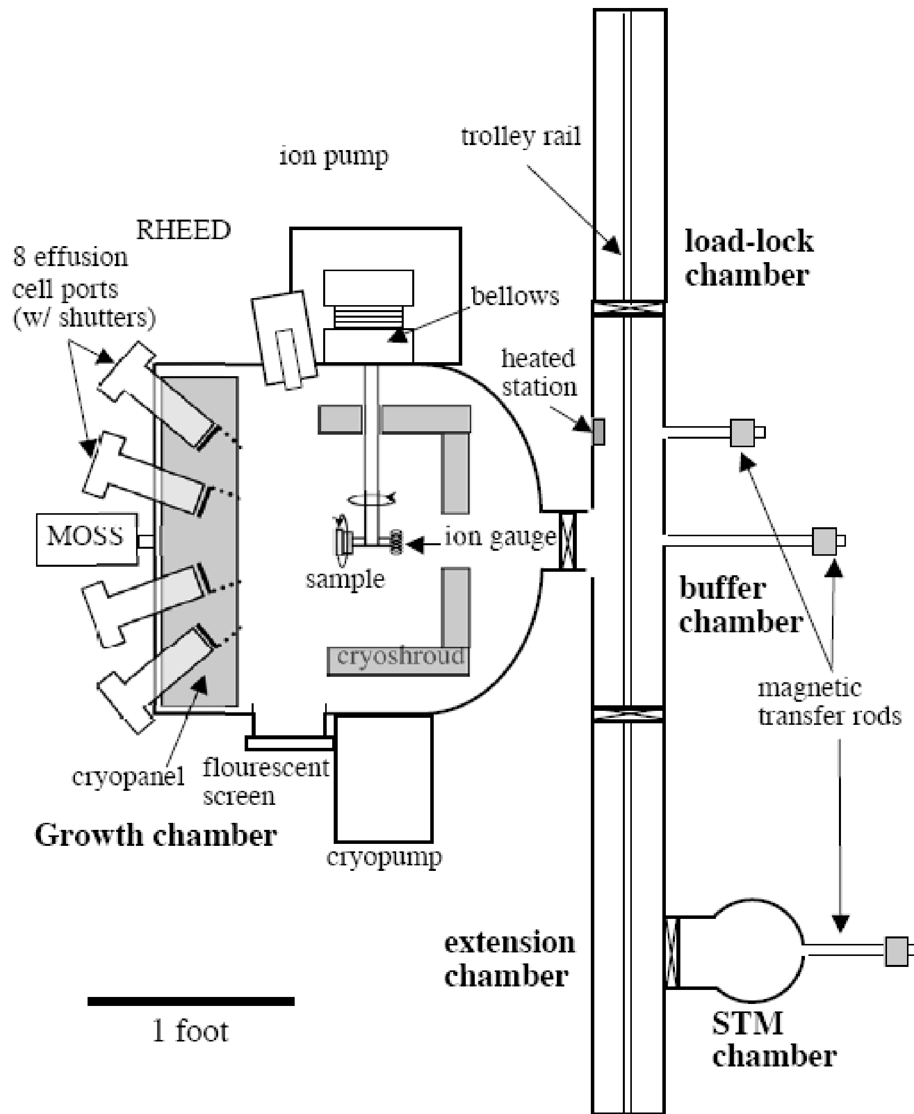

Figure 2.1: Schematic of the Modified Varian Gen II molecular-beam epitaxy system used to grow our samples. The system consists of a separately pumped growth chamber, buffer chamber, and load-lock. Samples are moved between sections using magnetic transfer rods and trolleys. The growth chamber source flange contains several sources (In, Ga, Al, Si, Te, and As), as well as an RF plasma source for the creation of active N. An additional source flange contains a (RGA) for *in-situ* mass spectroscopy. Computer controlled pneumatic shutters regulate the exposure of the samples to each molecular beam. During growth, samples are held in place by the CAR. This growth chamber contains facilities for *in-situ* reflection high-energy electron diffraction (RHEED) and a multi-beam optical stress sensor (MOSS).

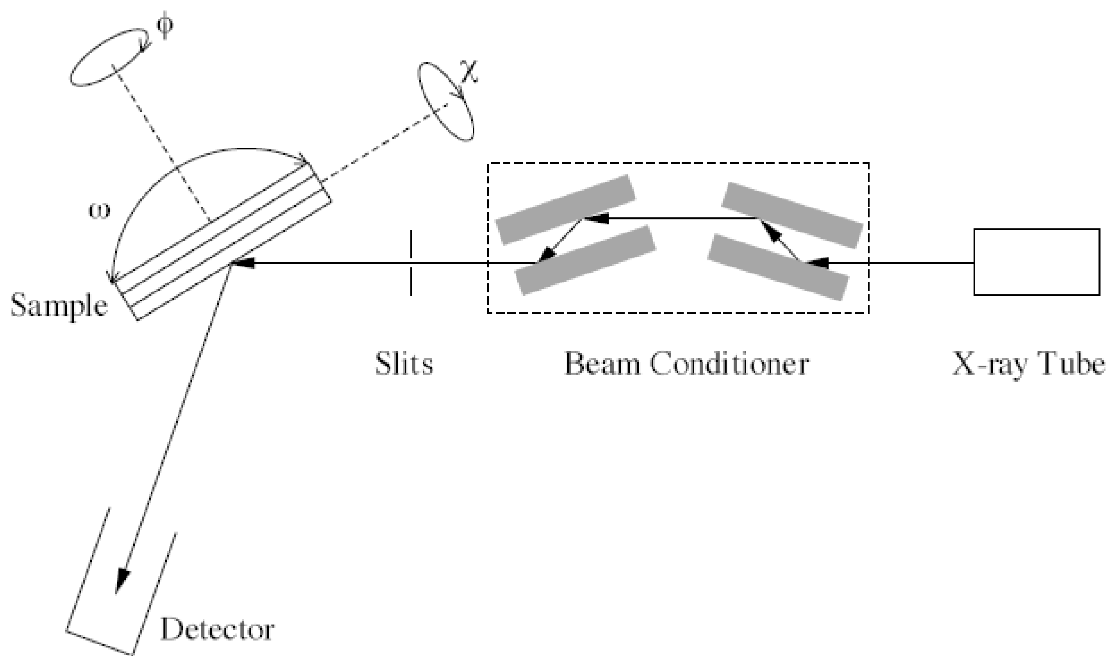

Figure 2.2: Schematic of the experimental setup of the BEDE D1 system for x-ray rocking curve measurements.

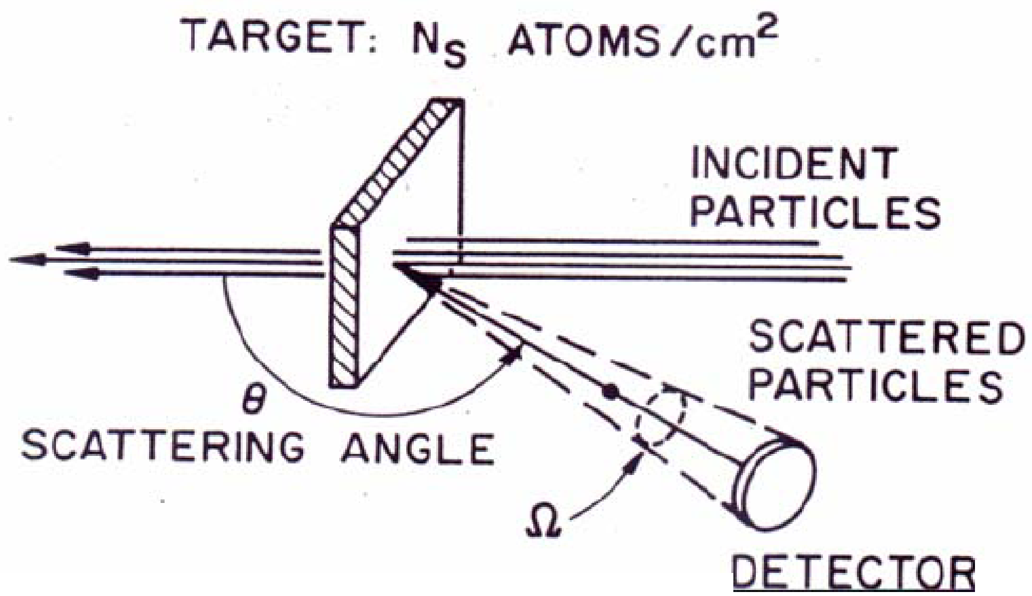

Fig. 2.3: Schematic diagram of the Rutherford backscattering spectroscopy experimental setup

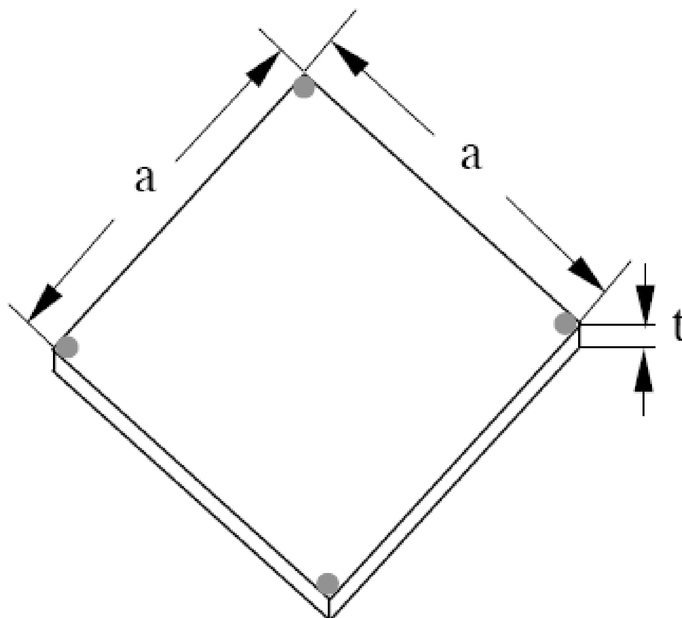

Fig. 2.4: Schematic of a typical symmetric van der Pauw specimen

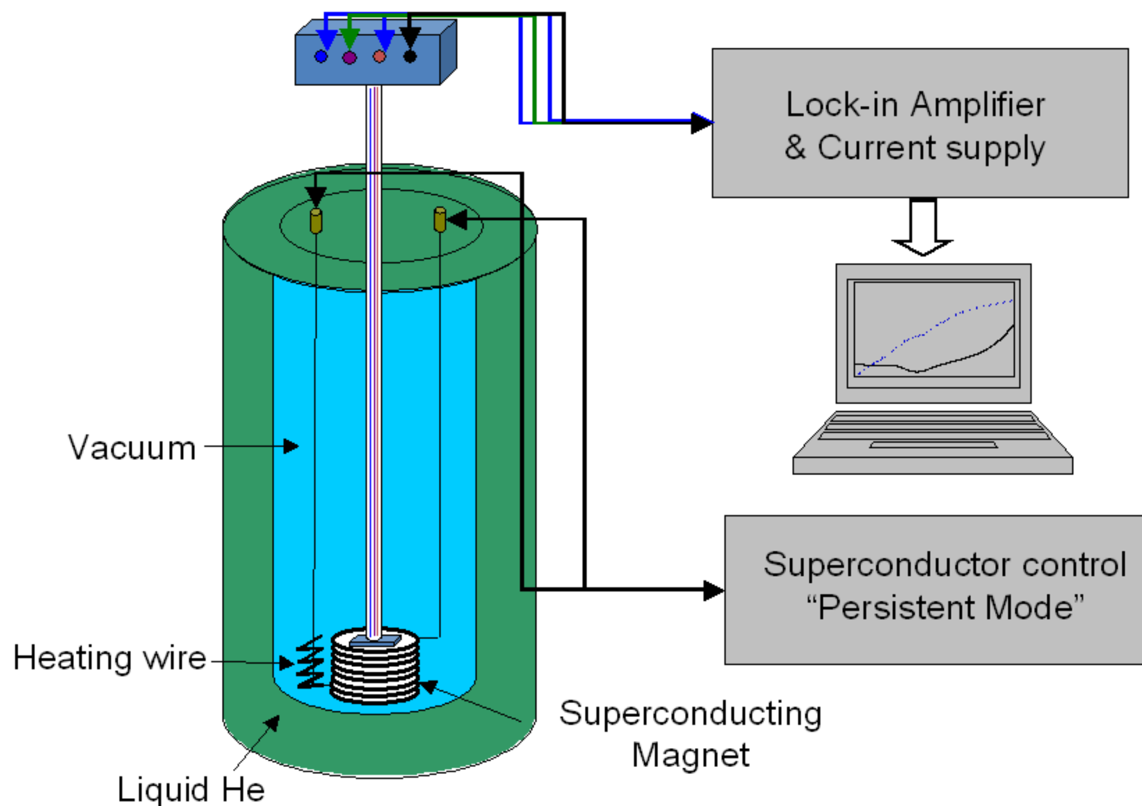

Figure 2.5: A schematic of the variable temperature cryostat used in the transport and PPC measurements. Samples were loaded into the sample chamber of the cryostat and kept the sample under vacuum. The next section of the cryostat is filled with liquid helium. The temperature is controlled by allowing small amounts of He gas, near liquid He temperatures, to flow through a valve in to the sample chamber, pumping on the sample chamber with the vacuum pump, and using a heating coil, which is controlled by a LakeShore 340 Temperature Controller. Inside the cryostat is a superconducting magnet, which is emmersed in liquid He and whose field was controlled by either a LakeShore Magnet Power Supply or a AMI Model 420 Power Supply along with a AMI Model 601 Energy Absorber.

3. RESULTS AND DISCUSSION

3.1 Overview

This chapter describes our investigations of the effect of interstitial N on the electronic properties of GaAsN alloy films. The correlation between annealing temperature, interstitial N fraction, and the transport properties of GaAsN are presented. In this work, it is shown that post-growth rapid thermal annealing (RTA) can be used to control the interstitial nitrogen fraction. Therefore, this treatment can be used to gain insight into the interstitial N-related degradation of the electronic and optical properties observed in GaAsN, and reveal the nature of interstitial N as an electron trapping and scattering center.

Chapter 1 summarized literature on the effect of N concentration and post-growth annealing on the electronic properties of dilute N GaAsN alloy films. The bulk of our work is devoted to understanding the effect of interstitial N on the electronic properties of GaAsN alloy films. We begin with ion beam analysis to quantify the interstitial N fraction in as-grown and annealed films. The transport properties are then investigated for films with various N concentrations. Interstitial N is shown to introduce a deep electron trapping level below the conduction band edge, leading to the deterioration of electronic properties in GaAsN films. Annealing reduces the concentration of these traps, leading to a significant improvement in both electron mobility and free carrier concentration in the films. Additionally, in GaAsN, a persistent photoconductivity (PPC) effect is observed and is suppressed by annealing. This suggests that the electron trapping and scattering

states, which cause the degradation of electronic properties and PPC in GaAsN, are due interstitial N.

3.2 Background

As described in Chapter 1, N may be incorporated into the GaAs lattice through several mechanisms. Due to the relatively small size of N, in comparison to As, a significant fraction of N atoms are predicted to sit on non-As-substitutional (N_{AS}) sites. Several possible configurations are shown are shown in Fig. 1.2. Thermodynamic calculations using the first-principles pseudopotential method, in the local-density approximation, have predicted that the binding energy of $(V_{Ga} - N_{As})_{nn}$ is 0.05 eV.[1, 2] Therefore, since the binding energy of $(V_{Ga} - N_{As})_{nn}$ is less than the energy of thermal vibrations, its concentration is predicted to be negligible. The calculated formation energies of the NN_{split}, NAs_{split}, and $(As_{Ga} - N_{As})_{nn}$ defects are 1.52 eV, 2.49 eV, and 1.96 eV, respectively. However, $(As_{Ga} - N_{As})_{nn}$ defects have not been experimentally observed by recent deep-level transient Fourier spectroscopy (DLTFS).[2] In addition, Zhang et al has suggested that the formation of Nitrogen split interstitials, $(NN)_{As}$ or $(NAs)_{As}$, can help release surface tension during growth and, thus, are energetically favorable.[2] Therefore, the dominant defect in GaAsN is predicted to be N split interstitials, namely NN_{split} and NAs_{split}.[2,3] Furthermore, Zhang et al predicts that interstitial N create deep defect energy levels below the conduction band.[4]

Since the electron and hole mobilities[5] and minority carrier lifetimes[6, 7] in $GaAs_{1-x}N_x$ and $In_yGa_{1-y} As_{1-x}N_x$ decrease with increasing x, it is likely that N interstitials also act

as carrier scattering centers. This leads to poor performance of devices such as solar cells and heterojunction bipolar transistors. [5-7]Thus, understanding the impact of N interstitials on the optical and electronic properties of the GaAsN alloys is critical to the development of dilute nitrides for device applications.

Post-growth rapid thermal annealing (RTA) has been extensively used to improve the photoluminescence (PL) efficiency of (In)GaAsN.[8-10] The improvement is commonly attributed to the elimination of some grown-in "competing nonradiative channels." However, the exact mechanism is not fully understood,[11,12,10] and reports on the effect of annealing on transport properties of (In)GaAsN are limited.[13,14] NRA is thus far the only direct method for determining f_{in} and, to date, there are two data points in literature comparing f_{in} in GaAsN before and after RTA.[15,16] Spruytte et al and Ahlgren at all used a combined nuclear reaction analysis and channeling technique to show substantial decreases in the interstitial N concentration, 10% and 3% respectively, after annealing.[15,16] Additionally, Krispin et. al use deep-level transient Fourier spectroscopy and assert that annealing at 720°C leads to the removal of $(NN)_{As}$.[1] Ramsteiner et. al assigned a Raman local vibrational mode to $(NN)_{As}$, and found its intensity was eliminated by annealing at 800°C.[17] However, the relationship between interstitial N incorporation and the electronic properties of GaAsN has not been reported.

3.3 Nitrogen Incorporation into GaAsN

3.3.1 Possible N out diffusion

Following the growth, high-resolution x-ray rocking curve (XRC) measurements were performed to determine nitrogen composition. Figure 3.1 shows (004) and (224) x-ray rocking curves for $GaAs_{1-x}N_x$ with x=0.017, N both before and after annealing, shown in black and red, respectively. Analysis of a series of (004) and (224) XRCs indicates that the epilayer peak position for both (004) and (224) remain constant after RTA up to 760°C for 60s annealing. Thus, the N composition in the GaAsN films remains unchanged after RTA, suggesting the change in electronic properties is unlikely a result of N out-diffusion.

3.3.2 N Interstitial Incorporation

Ion beam analysis provides quantitative evidence for the presence of interstitial N in GaAsN and, thus far, NRA is the only direct method for determining f_{in} Shown in Fig. 3.2 is the concentration of interstitial N versus total N concentration for many GaAsN samples grown and measured previously by our group,[18] (squares and stars), as well as measurements by Spruytte et al.,[15] (triangles), and Ahlgren, et al.[16] (Circles). In general, a trend of increasing interstitial N concentration with increasing total N concentration is apparent. For low T (high T) growth of GaAsN ~20% (~45%) of N is incorporated interstitially, illustrated by the dashed black and blue lines, respectively, in Fig. 3.1.

Furthermore, we have observed an RTA induced decrease in the interstitial fraction from 18% to 11% and 16% to 10% in GaAsN films grown with N compositions of 0.5% and 1.3%, respectively, shown in Table 3.1 and represented by the stars in Fig. 3.1. To date, there are two data points in literature comparing f_{in} in GaAsN before and after RTA, depicted as squares and circles in Fig. 3.1.[15, 16] This is strong evidence that annealing reduces the interstitial N fraction in GaAsN alloys.

Shown in Fig. 3.3 is the room temperature Raman spectra for a $GaAs_{0.981}N_{0.019}$:Si film before and after annealing. Both spectra show features arising from GaAs-like longitudinal-optical (LO) and transverse-optical phonons from 500 to 580cm^{-1}, and GaN like LO phonons at 470cm^{-1}. For the as-grown film, local vibration modes at frequencies 410 and 420 cm^{-1} are detected, which are attributed to N dimers on Ga site $(NN)_{Ga}$ and As site $(NN)_{As}$, respectively.[17] The intensities of the modes associated with interstitial N were significantly reduced after RTA. As discussed earlier, we provide direct evidence of the reduction in f_{int} by the NRA, thus providing the first direct evidence that these Raman signatures are due to N interstitials.

Our work with ion beam analysis and Raman spectroscopy suggests that annealing can be used as a means to control the fraction of interstitial N in GaAsN samples. This affords us a means study the correlation between the change interstitial N fraction and the change electronic properties of GaAsN. In the rest of this chapter annealing temperature will be used to as a knob to examine the effect of N interstitials on GaAsN alloy films.

3.4 Transport Properties of GaAsN

Figure 3.4 shows the free carrier concentration vs. reciprocal temperature for as-grown $GaAs_{0.981}N_{0.019}$:Si film and $GaAs_{0.981}N_{0.019}$:Te films, in comparison with an as-grown GaAs:Te film. For GaAs:Te, [n] is temperature-independent in the temperature range 50 to 300K, which is typical of degenerate semiconductors.[6] For the as-grown GaAsN films in Fig. 3.4, we observe two distinct temperature regimes with drastically different temperature dependences above and below 150K. At $T < 150K$, [n] is apparently temperature independent and carriers are likely due to shallow donors, which we define as [n_s]. In the region $T > 150K$, a thermally activated increase in carrier concentration is apparent, suggesting the presence of a deep level within the GaAsN bandgap. The temperature dependence of the free carrier concentration in GaAsN films is very similar to what has been observed in n-type AlGaAs, where two T dependent regimes of [n] are observed, and are attributed to the co-existence of a shallow donor and a deep DX-center donor.[19-22] The similarity suggests the presence of two donor levels in the GaAsN bandgap, one being a shallow donor and the second a thermally-activated deep donor. Since this temperature dependence of [n] is observed in GaAsN films, but not the GaAs control samples, the deep donor is likely related to the presence of N. We also notice that [n] continues to increase even at room temperature, suggesting that the deep donor level has a large activation energy.

To extract the activation energy of the N-related deep donor level, E_{dd}, we employ the expression for semiconductors with two distinct donor levels,

$$\sqrt{n(n-n_S)} \propto \exp(-\frac{E_N}{2k_B T}) \quad (1),$$

where k_B is Boltzmann constant, n is the apparent carrier concentration, and n_s is the saturated shallow donor concentration.[6] Using this model, the activation energy of the deep-level E_{dd}, is determined to be about 60, 85, 95 meV for as-grown GaAsN films with 1.9, 1.6, 1.2% N, respectively. These are much greater than the activation energy of hydrogen-like shallow donor levels in GaAs, typically 5-6 meV, further suggesting the presence of a second deep donor. Thus, these donors act as carrier trapping centers, leading to the low [n] and μ observed in as-grown GaAsN films. In addition, it is worth noting that E_{dd} decreases with increasing N composition, which can be explained by the picture that the band gap of GaAsN decrease with increasing N composition, while the N-related defect level remains unchanged.[1, 2, 23-25] The N-related shallow donor defect level discussed above may correspond to the shallow electron traps in GaAsN reported earlier. For example, using capacitance spectroscopy, Krispin et al found a composition independent electron trap about 1.1eV above the valence band edge.[1] Kurtz el al found a trap 0.18 to 0.25eV below the conduction-band edge by DLTS[23]. Kaplar et al used DLTS to reveal shallow electron traps with an activation energy of 0.14eV in Sn-doped n-type GaInNAs using DLTS. In addition, first principles calculations suggest the existence of N-related defect states below GaAsN conduction band, whose positions are independent of with N composition.[2, 24, 25]

Figure 3.5 shows the free carrier concentration as a function of reciprocal temperature for as-grown and annealed $GaAs_{0.981}N_{0.019}$:Te films, in comparison with as-grown GaAs:Te. To determine E_{dd}, we plot $\sqrt{n(n-n_S)}$ vs. inverse temperature for each annealing temperature, shown as open circles in Fig. 3.5. Analysis of Eq (1) reveals E_{dd} is essentially independent of annealing temperature, suggesting the energy of the defect

level with respect to the conduction band edge is unaffected by the annealing. We can again compare this to the to the case of DX-centers in AlGaAs. The activation energy of the deep DX-donor in AlGaAs is independent of the Al mole fraction, but the relative concentration decreases with decreasing Al mole fraction, while the shallow donor concentration increases. This similarity suggests that annealing reduces the concentration of N-related trap centers in GaAsN films, thus, leading to an increase in free carrier concentration.

For GaAsN:Te films annealed at 780°C, [n] is essentially temperature independent. Additionally, we observe a remarkable increase in [n_s] with increasing annealing temperature. Since [n_s] increases and [n] becomes less temperature dependent with increasing annealing temperature, it is likely that annealing reduces the fraction of carriers captured by the deep-level defects, presumably do to a reduction in the concentration of N-related trapping centers.

3.5 Persistent Photoconductivity

3.5.1 Existence of PPC

Shown in Fig. 3.6 is the typical normalized photoconductivity, g_t^N, of a GaAsN film plotted as a function of time, before and after illumination, measured at 11K. For the purpose of analysis, the moment that the LED is turned off is set to be t=0. g_t^N is defined as

$$g_t^N = \frac{g_t - g_d}{g_0} = (\frac{1}{\rho_t} - \frac{1}{\rho_d}) / \frac{1}{\rho_0}, (2)$$

where ρ_d is the resistivity in measured in the dark, ρ_0 is the resistivity at t=0 and ρ_t is the resistivity at time t after illumination. g_d, g_0 and g_t are the inverses of ρ_d, ρ_0 and ρ_t, respectively. Shown in Fig. 3.5, for t=4 hours after illumination, the decrease in g_t^N is less than 5%, indicating the existence of PPC in GaAsN films.

3.5.2 Determining the Potential Barrier in GaAsN

In Fig. 3.7, [n] and μ, measured both in the dark and after illumination, are plotted as a function of measurement temperature, as described in section 2.7. For T>90K, each measurement can be treated as a snap shot of meta-stable state due to the fast decay at these temperatures. As shown in Fig. 3.7, at temperatures below 40K, [n] and μ increase by a factor of 3 and 2 for [n] and μ, respectively, with illumination. As temperatures rise above 120K, [n] and μ relax quickly to their dark measurement value. For temperatures greater than 160K, very weak PPC effect was observed. This behavior is expected, since, as the temperature increases, a larger number of photo-generated carriers have thermal energy large enough to overcome the potential barrier and relax to the equilibrium state.

Figure 3.8, shows the resistivity as a function of time after turning off the LED, measured at different temperatures. At low temperature, after an initial increase in the first ~10 sec, the resistivity increases slowly with time, indicating the presence of PPC. On the other hand, at high temperature, the resistivity increases substantially after turning off the illumination, almost recovering to the dark resistivity value, indicating the

disappearance of the PPC effect at high temperatures. The large dynamic range of PPC effect enables us to study the decay kinetics of photo-generated conductivity in GaAsN films. We can therefore extract the characterization potential barrier, which is termed capture energy, E_c, by Watanabe et al in DX-center theory, of the N-related defect. In order to consider the stretched-exponential relaxation model, $g_t^N = \exp(-(\frac{t}{\tau})^\beta)$, where τ is the characterization decay time and β is an index, the normalized conductivity of $GaAsN_{.013}$ as a function of time is plotted as $Ln(Ln(1/g_t^N))$ vs $Ln(t)$, shown in Fig. 3.9. Relaxations described by stretched-exponentials are commonly observed in disordered systems, and the deviation from standard exponential decay is usually the result of a distribution of barrier energies.[26, 27] The linear behavior of the data suggests that the decay mechanism of PPC in GaAsN can be well described by the stretched-exponential relaxation model. For each temperature, we have used linear least-squares fits to the experimental data to determine τ and β. We find that τ decreases rapidly with increasing temperature, presumably because the probability of activation of the localized carriers to overcome the potential capture barrier increases with increasing temperature. Thus, the capture time exhibits Arrhenius behavior, described by $\tau = \tau_0 \exp(\frac{E_c}{K_B T})$, where τ_0 is the high temperature limit of τ, and E_c is the PPC capture energy barrier. Form the slope of the plot in Fig. 3.10, the resulting capture energy barrier, E_c, was determined to be 340 and 250 meV for $GaAs_{987}N_{.013}$ and $GaAs_{.981}N_{.019}$, respectively. Additional studies suggest that the PPC effect in GaAsN is eliminated by RTA.[28, 29] This further suggests that the electron trapping states associated with the PPC effect are also related to N interstitials, which are removed by annealing.

Further experimental studies are required to determine the microscopic configuration and energy level positions of N interstitials in GaAsN alloys. We propose that the PPC effect in (In)GaAsN is due to the incorporation of interstitial N, which presumably acts as a deep electron trapping level, that can be optically ionized by illumination. Due to a capture energy barrier, at low temperatures the excited carriers cannot go back to the trap state; therefore, the increase in [n] and μ persists. At high temperature (T>100K), the thermal energy of the excited carriers is large enough to conquer the capture barrier, and PPC effect starts to disappear.

3.5.3 Mobility vs. Free Carrier Concentration in GaAsN

Additionally, the PPC effect in GaAsN at low temperature provides a unique opportunity to probe μ as a function of n at fixed temperatures, without having to grow multiple samples with different doping concentrations. This has the potential to provide valuable information on the N-related carrier scattering mechanism. Plotted in Fig. 3.11 is the electron μ as a function of [n] at two fixed temperatures. At 40K, μ increases monotonically from 50 to 140 cm^2/Vs as [n] is increased from 2.2 to $4x10^{17}$ cm^{-3}. A similar trend is observed at 80K with a shift to higher values of μ at all [n].

The increase of μ with [n] serves as evidence for the mobility edge picture.[30,29] In this picture, the N-related defects, in particular, interstitial N-related defects induce localized states near the conduction band edge. When the Fermi level lies within the mobility edge, the free carriers experience strong scattering, resulting in very low μ. After illumination, [n] increases and Fermi level moves into the conduction band, the

carrier transport mechanism cross over from hopping conduction between localized states to extended band-like conduction, resulting in the significant increase in μ.

3.6 Discussion.

In this chapter we presented a study of the effect of interstitial N on the electronic properties of GaAsN. Films were investigated using a combination of variable temperature magnetoresistance and optical transient measurements, along with ion beam analysis and Raman spectroscopy. Ion beam analysis suggests that RTA reduces f_{in} in GaAsN alloys. Thus, we have provided the first direct evidence that local vibration modes attributed to N dimers on Ga site and As site in Raman spectroscopy are due to N interstitials. The reduction is presumably due to annealing assisted diffusion of N interstitials to As vacancies, thus reducing interstitial N fraction.

In the as-grown films, the free carrier concentration increases exponentially with increasing measurement temperature up to room temperature, suggesting the presence of N-related electron trapping defect with E_a about 60-95meV below the bandgap. After annealing this level is substantially suppressed. In addition, annealing substantially increases the free carrier concentration and electron mobility of GaAsN. Furthermore, PPC in GaAsN has been observed and the, and the optical capture barrier of this defect is determined to be 340-250 meV by variable temperature transient time measurement.

3.7 References

[1]P. Krispin, V. Gambin, J. S. Harris, and K. H. Ploog, Journal of Applied Physics **93,** 6095 (2003).
[2]S. B. Zhang, and S.-H. Wei, Phys. Rev. Lett. **86,** 1789 (2001).
[3]J. E. Lowther, S. K. Estreicher, and H. Temkin, Appl. Phys. Lett. **79,** 200 (2001).
[4]S. B. Zhang, and S. H. Wei, Physical Review Letters **86,** 1789 (2001).
[5]D. J. Friedman, J. F. Geisz, and A. J. Ptak, (Taylor & Francis, 2004), pp. pp. 371-394.
[6]J. F. Geisz, D. J. Friedman, J. M. Olson, S. R. Kurtz, and B. M. Keyes, J. Cryst. Growth **195,** 401 (1998).
[7]D. Kwon, R. J. Kaplar, S. A. Ringel, A. A. Allerman, S. R. Kurtz, and E. D. Jones, Appl. Phys. Lett. **74,** 2830 (1999).
[8]W. K. Loke, S. F. Yoon, S. Z. Wang, T. K. Ng, and W. J. Fan, Journal of Applied Physics **91,** 4900 (2002).
[9]I. A. Buyanova, G. Pozina, P. N. Hai, N. Q. Thinh, J. P. Bergman, W. M. Chen, H. P. Xin, and C. W. Tu, Applied Physics Letters **77,** PII [S0003 (2000).
[10]L. H. Li, Z. Pan, W. Zhang, Y. W. Lin, Z. Q. Zhou, and R. H. Wu, Journal of Applied Physics **87,** 245 (2000).
[11]I. A. Buyanova, G. Pozina, P. N. Hai, N. Q. Thinh, J. P. Bergman, W. M. Chen, H. P. Xin, and C. W. Tu, Applied Physics Letters **77,** 2325 (2000).
[12]Q. D. Zhuang, A. Krier, and C. R. Stanley, Journal of Applied Physics **101,** (2007).
[13]F. Ishikawa, G. Mussler, K. J. Friedland, H. Kostial, K. Hagenstein, L. Daweritz, and K. H. Ploog, Applied Physics Letters **87,** (2005).
[14]K. Volz, J. Koch, B. Kunert, and W. Stolz, Journal of Crystal Growth **248,** 451 (2003).
[15]S. G. Spruytte, C. W. Coldren, J. S. Harris, W. Wampler, P. Krispin, K. Ploog, and M. C. Larson, Journal of Applied Physics **89,** 4401 (2001).
[16]T. Ahlgren, E. Vainonen-Ahlgren, J. Likonen, W. Li, and M. Pessa, Applied Physics Letters **80,** 2314 (2002).
[17]M. Ramsteiner, D. S. Jiang, J. S. Harris, and K. H. Ploog, Applied Physics Letters **84,** 1859 (2004).
[18]M. Reason, H. A. McKay, W. Ye, S. Hanson, R. S. Goldman, and V. Rotberg, Applied Physics Letters **85,** 1692 (2004).
[19]E. F. Schubert, J. Knecht, and K. Ploog, Journal of Physics C-Solid State Physics **18,** L215 (1985).
[20]
[21]M. O. Watanabe, K. Morizuka, M. Mashita, Y. Ashizawa, and Y. Zohta, Japanese Journal of Applied Physics Part 2-Letters **23,** L103 (1984).
[22]N. Chand, T. Henderson, J. Klem, W. T. Masselink, R. Fischer, Y. C. Chang, and H. Morkoc, Physical Review B **30,** 4481 (1984).
[23]S. R. Kurtz, A. A. Allerman, E. D. Jones, J. M. Gee, J. J. Banas, and B. E. Hammons, Applied Physics Letters **74,** 729 (1999).
[24]A. Lindsay, and E. P. O'Reilly, Phys. Rev. Lett. **93,** (2004).
[25]P. R. C. Kent, and A. Zunger, Physica Status Solidi B-Basic Research **228,** 253 (2001).
[26]A. S. Dissanayake, J. Y. Lin, and H. X. Jiang, Physical Review B **48,** 8145 (1993).

[27]R. G. Palmer, D. L. Stein, E. Abrahams, and P. W. Anderson, Physical Review Letters **53,** 958 (1984).
[28]S. H. Hsu, W. R. Chen, Y. K. Su, R. W. Chuang, S. J. Chang, and W. C. Chen, Journal of Crystal Growth **290,** 87 (2006).
[29]Y. Jin, thesis, University of Michigan, In Preparation
[30]S. R. Kurtz, N. A. Modine, E. D. Jones, A. A. Allerman, and J. F. Klem, Semiconductor Science and Technology **17,** 843 (2002).

3.8 Tables and Figures

N composition (%)	RTA	f_{int}
0.5	as-grown	18%
	annealed	11%
1.3	as-grown	16%
	annealed	10%

Table 3.1: interstitial nitrogen fraction for GaAsN films before and after annealing determined by Rutherford backscattering spectrometry and nuclear reaction analysis.

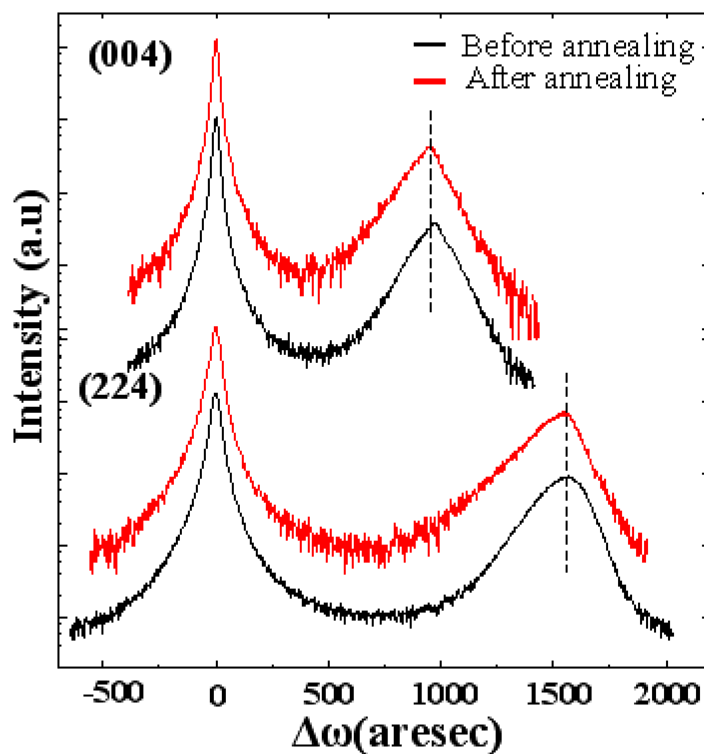

Fig. 3.1: X-ray diffraction curves for the symmetric (004) and the asymmetric and the glancing-incidence (224) of a GaAsN sample with 1.7% N. The curves Analysis of a series of (004) and (224) XRCs indicates that the epilayer peak positions remain the same after RTA up to 760°C for 60s annealing. Thus the N compostition remains constant.

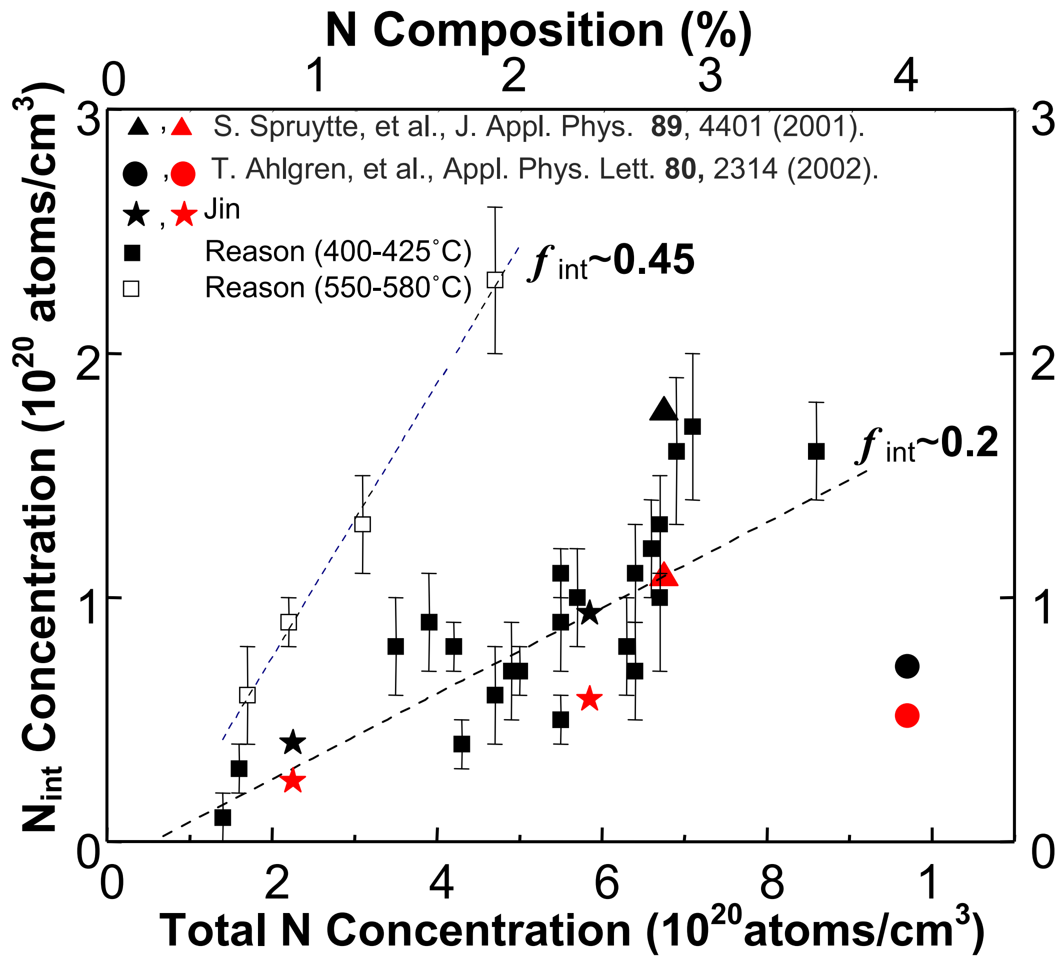

Fig. 3.2: Interstitial N measurements made on GaAsN samples using Ion beam analysis by Spruytte and et al., Ahlgren, et al., as well as previously by our group, both for low and high T growth. Measurements were made The interstitial fractions for low and high T growth are shown by the dashed black and blue lines, respectively. For low T (high T) growth of GaAsN ~20% (~45%) of N is incorporated interstitially.

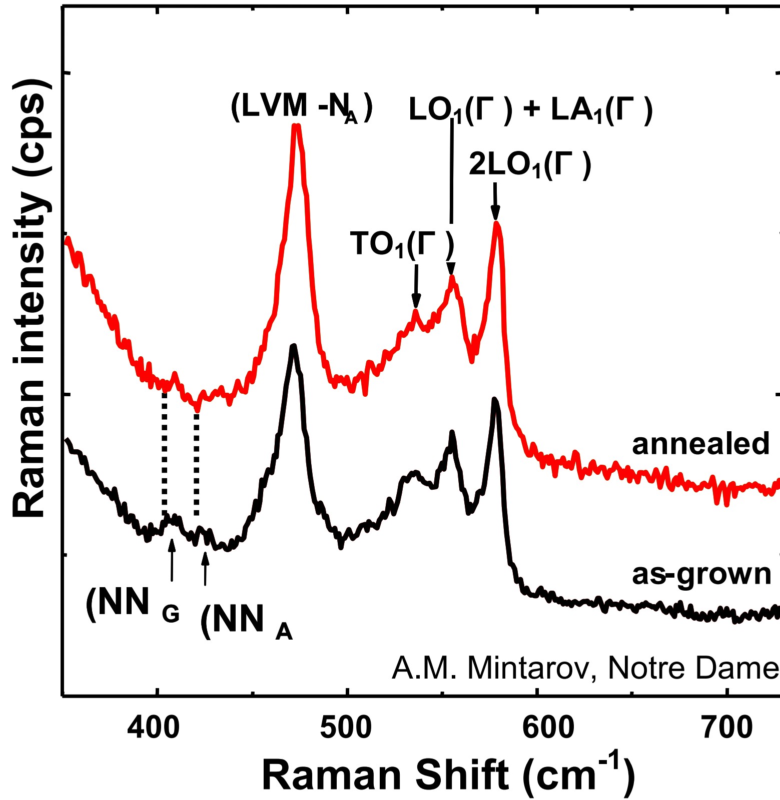

Fig 3.3: Unpolarized Raman spectra of $GaAs_{0.981}N_{0.019}$:Si in the range of substitution (LO_2) and interstitial nitrogen induced vibrations. Both spectra show features arising from GaAs-like longitudinal-optical (LO) and transverse-optical phonons from 500 to 580cm^{-1}, and Ga-N like LO phonons at 470cm^{-1}. In addition, we observed Raman features at frequencies 410 and 420 cm^{-1}, the intensities of which are significantly suppressed after RTA. The reduction in f_{int} observed by NRA suggests these Raman signatures are attributed to N interstitials.

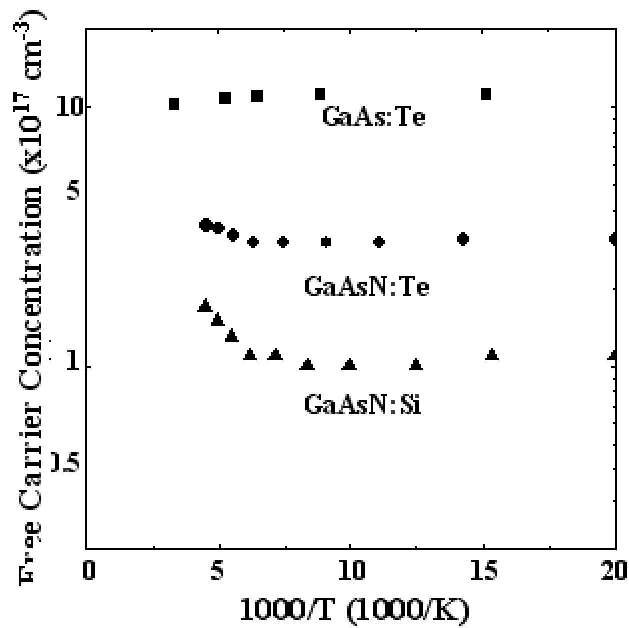

Fig. 3.4 : Free carrier concentration as a function of inverse temperature for as-grown $GaAs_{0.981}N_{0.019}$:Si film and $GaAs_{0.981}N_{0.019}$:Te films

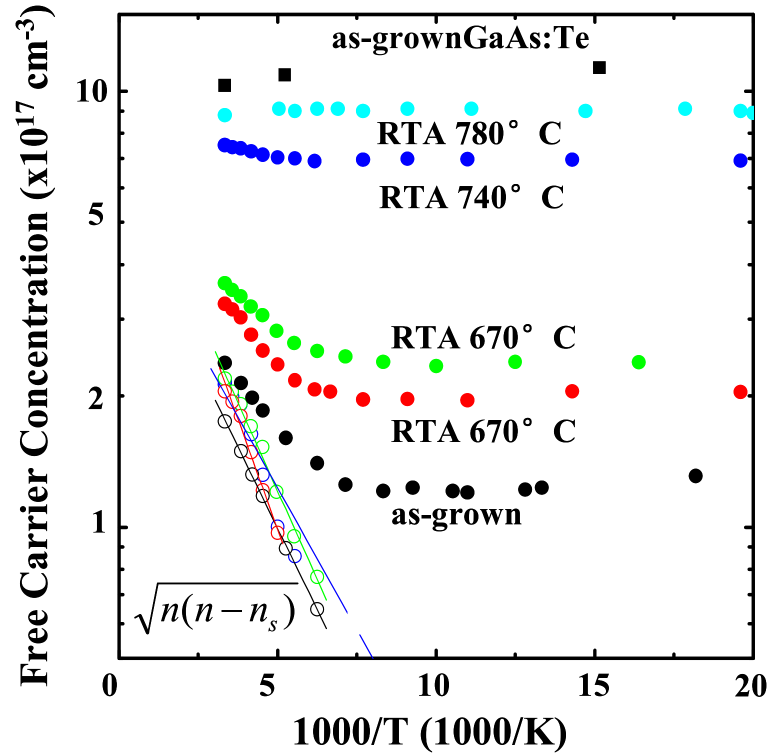

Fig. 3.5. Free carrier concentration, [n], as a function of inverse temperature for $GaAs_{0.987}N_{0.013}$:Te films annealed at different temperatures. Two distinct T dependent regimes of [n] are apparent: T>150K, [n] increases exponentially with increasing T; T< 150K, [n] is independent of T. In order to use a 2-level system formalism to extract the activation energy of N-induced deep donor state, $\sqrt{n(n-n_S)}$ is also plotted in open circles for [n]>[n_s].

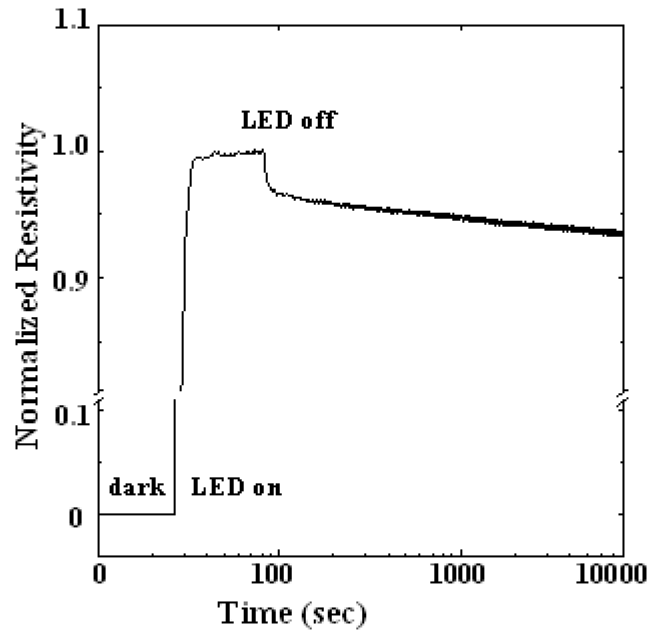

Fig 3.6: A typical normalized photoconductivity, g_t^N, of a GaAsN film plotted as a function of time before and after illumination, measured at 11K.

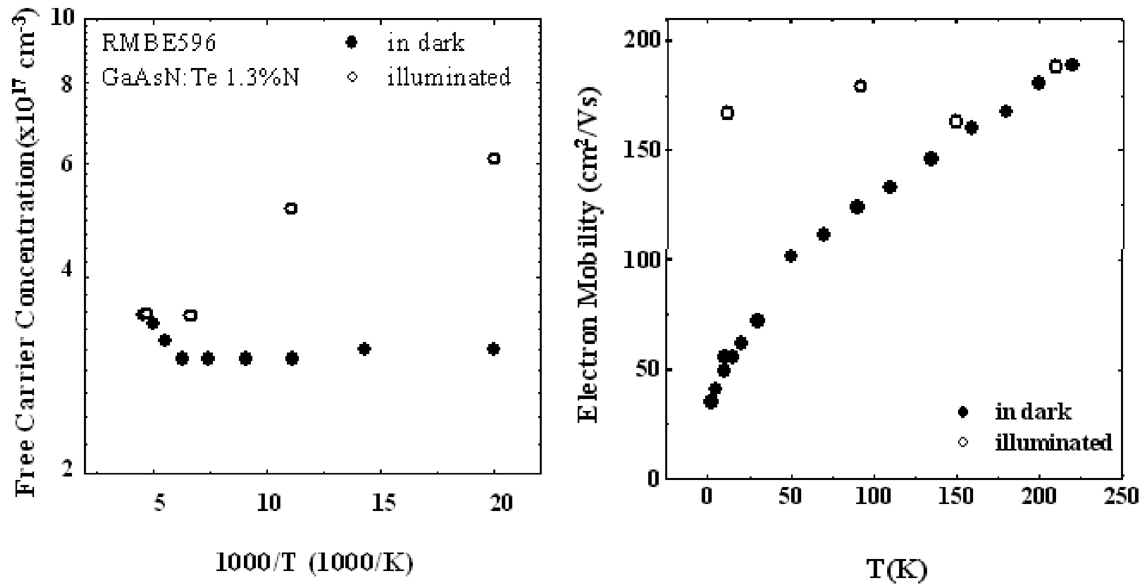

Fig 3.7: The free carrier concentration, [n], and electron mobility, μ, as a function of measurement temperature, both in dark and 5min after illumination is turned off, since the sample is in metastable state after the illumination is turned off. In dark, [n] decrease with temperature in the beginning and saturates at low temperature, as describe before. At the same time, μ decreases with temperature in the whole temperature, which are typical for GaAsN as-grown films. As shown by the open circles, illumination causes a persistent increase of the carrier concentration and mobility at low temperatures.

Fig 3.8: The resistivity as a function of time after turning off the illumination measured at different temperatures.

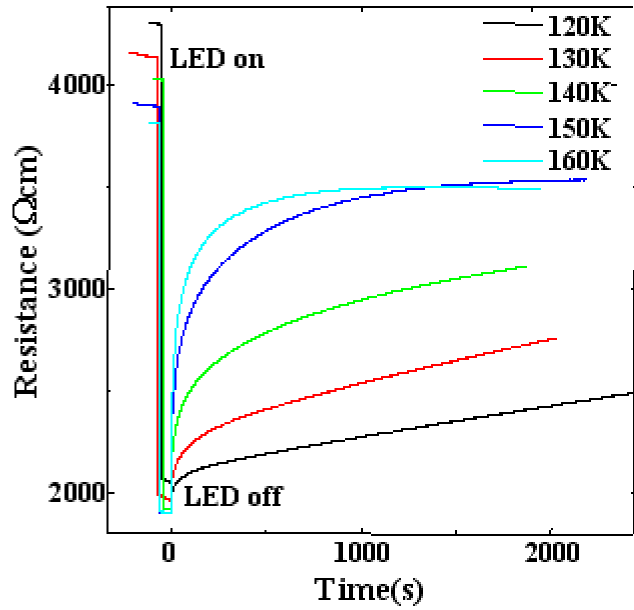

Fig 3.9: The resistivity is converted to normalized conductivity and ln(ln(G(t)/G(0)) is plotted as a function of ln(t) for $GaAsN_{1.3}$ film at various temperatures.

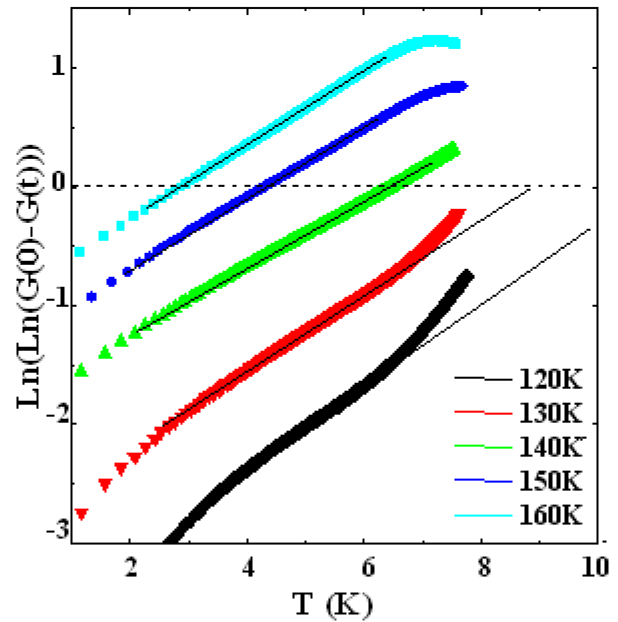

Fig 3.10: The decay time constant plotted according to the Arrhenius equation.

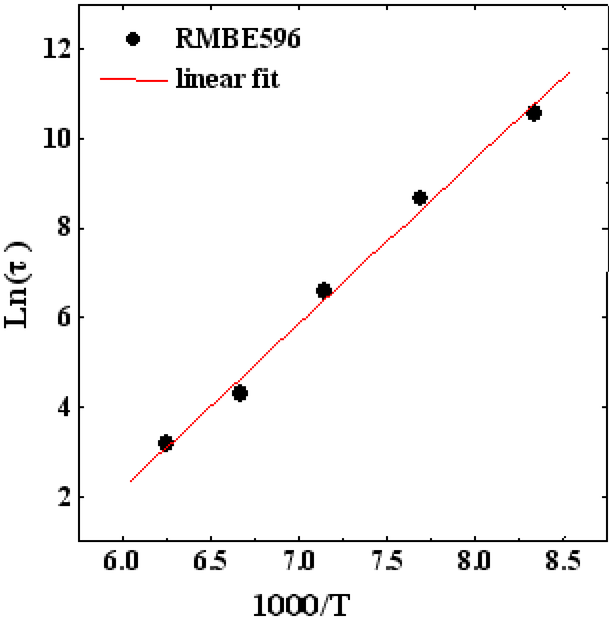

Figure 3.11: Mobility, μ, as a function of free carrier concentration, [n].

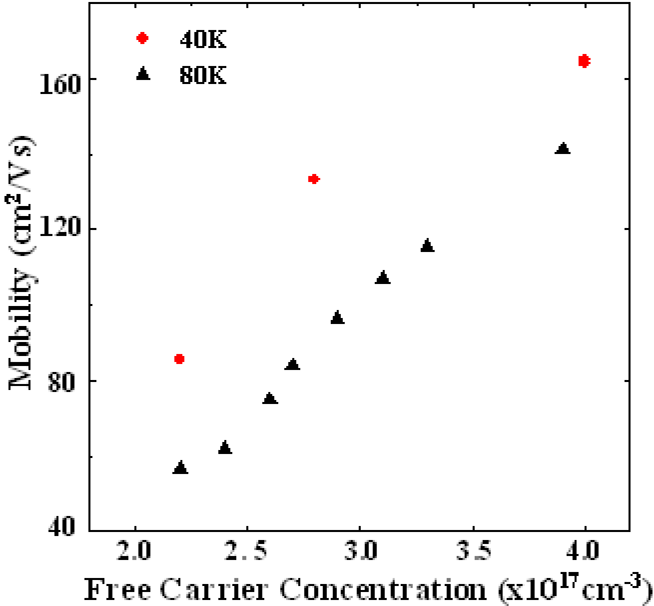

4. SUMMARY AND FUTURE WORK

4.1 Summary

In summary, we have used RTA to investigate the influence of N interstitials on the electronic properties of GaAsN alloy films. Nuclear reaction analysis reveals an RTA-induced decrease in the concentration of N interstitials, while the total N concentration remains constant. Corresponding signatures for the reduction in interstitial N concentrations are also apparent in Raman Spectra. This suggests that RTA reduces f_{in} in GaAsN alloys, presumably due to annealing assisting interstitial N diffusion to As vacancies. Therefore, we have utilized RTA as a knob to control interstitial N concentration and examine the influence of interstitial N on the electronic properties of GaAsN alloy films.

Hall and resistivity measurements reveal a significant increase in [n] and μ after RTA. In addition, temperature dependent transport measurements reveal a thermally activated increase in free carrier concentration at higher measurement temperatures, suggesting the presence of a carrier trapping level below the GaAsN conduction band edge. This temperature dependence is suppressed upon annealing, indicating a reduction in the concentration of the electron trapping defects after annealing. The increase in [n] following RTA suggests the association of the defects with interstitial N. In addition, PPC effect has been observed in GaAsN, and the capture energy barrier of this defect is determined by variable temperature transient time measurement. The PPC effect is

suppressed by annealing, further suggesting a correlation between the interstitial N defect states and the electronic properties in (In)GaAsN.

4.2 Suggestions for Future Work

Several suggestions are made for future work as follows. Further studies on the effect of annealing on the PPC effect would be interesting, such as the influence of f_{in} on the capture barrier energy in GaAsN alloys. Also, further studies to explicitly characterize the microscopic picture of the N-interstitials will be helpful to understanding its influence on the electronic properties of GaAsN.